Università degli Studi di Ferrara

DOCTORAL COURSE IN
"PHYSICS"

CYCLE 38

COORDINATOR Prof. Paolo Lenisa

STUDY OF THE INJECTION SYSTEM AND DEVELOPMENT OF A BUNCHER DEVICE FOR THE CYCLOTRON OF SPES PROJECT AT LABORATORI NAZIONALI DI LEGNARO

SCIENTIFIC/DISCIPLINARY SECTOR (SDS) FIS/01

CANDIDATE

Dr. Arturo Abbondanza

SUPERVISORS

Dr. Mario Maggiore

Dr. Piergiorgio Antonini

Dr. Andrea Gottardo

YEARS 2022/2025

ABSTRACT

At Laboratori Nazionali di Legnaro, a new facility for nuclear physics called SPES (Selective Production of Radioactive Species) is under construction. The aim of the project is to produce radioactive isotopes for fundamental research in nuclear structure and for applications, such as nuclear medicine. The core of the facility is a cyclotron supplied by Best Theratronics, able to produce two proton beams with energies from 35 to 70 MeV and maximum total current intensity of 700 μA. A key feature of this machine is the high current intensity that will be necessary, once completed the infrastructure, for a large production of radioisotopes.

The present study aims at investigating the mechanisms of beam injection into the SPES cyclotron, to optimize the injection process, to reduce particle losses and to increase the injected beam current in the machine. Based on the literature review, a buncher device is the ideal choice to improve the injection efficiency.

Part of the present work is devoted to numerical simulations, developed using the Simion software package, of the H^- ion beam dynamics in the injection line, as it is actually in operation without the buncher device, and in the central part of the cyclotron, where a probe is located for the measurement of the beam current intensity. The reliability of the simulations is demonstrated by comparison with the experimental data collected during cyclotron operations.

The virtual model of the injection line and the central part of the cyclotron is then used to evaluate the performance of the buncher device that will be installed in a specific position along the injection line. The simulation results show a possible noticeable increase (approximately by factor 2) in the beam current injected into the cyclotron. Additionally, the effect of space charge due to non-negligible beam current is taken into account to estimate the possible reduction in the injection improvement.

After the simulation of the component, the design of a possible implementation of the electronics chain required for the buncher operation is

described, including the electronic signal generation and amplification, and the impedance matching with the device.

In conclusion, the present work investigates the beam dynamics in the injection line and in the central region of the SPES cyclotron. To optimize the injection efficiency a buncher device is designed, whose performance is estimated by means of numerical simulations. A possible realization of the electronics necessary to its reliable operation is finally proposed.

SOMMARIO

Presso i Laboratori Nazionali di Legnaro è in costruzione un nuovo impianto per la fisica nucleare denominato SPES (Selective Production of Radioactive Species). L'obiettivo del progetto è la produzione di isotopi radioattivi per la ricerca fondamentale in struttura nucleare e applicazioni, come la medicina nucleare. Il cuore dell'impianto è un ciclotrone fornito da Best Theratronics, in grado di produrre due fasci di protoni con energie da 35 a 70 MeV e un'intensità di corrente massima totale di 700 μA. Un aspetto chiave di questa macchina è l'elevata intensità di corrente estratta, che sarà necessaria, una volta completata l'infrastruttura, per la produzione su larga scala di radioisotopi.

Il presente studio si propone di indagare i meccanismi di iniezione del fascio di ioni H^- nel ciclotrone SPES, con l'obiettivo di ottimizzare il processo di iniezione, riducendo le perdite di particelle e aumentando la corrente del fascio iniettato nella macchina. Sulla base della revisione della letteratura, un dispositivo "buncher" si rivela la scelta ideale per migliorare l'efficienza di iniezione.

Parte del presente lavoro è dedicata a simulazioni numeriche, sviluppate utilizzando il software Simion, della dinamica del fascio nella linea di iniezione, come è in operazione attualmente, e nella regione centrale del ciclotrone, dove è posizionata una sonda per la misura dell'intensità di corrente del fascio. L'affidabilità delle simulazioni viene dimostrata dal confronto con i dati sperimentali raccolti durante le operazioni del ciclotrone.

Il modello virtuale della linea di iniezione e della regione centrale del ciclotrone viene quindi utilizzato per valutare le prestazioni del dispositivo "buncher" che verrà installato in una posizione specifica lungo la linea di

iniezione. I risultati della simulazione mostrano un possibile aumento significativo (circa un fattore 2) della corrente del fascio iniettata nel ciclotrone. Inoltre, viene preso in considerazione l'effetto della carica spaziale dovuto a una corrente del fascio non trascurabile per stimare la possibile riduzione nel miglioramento dell'iniezione.

Dopo la simulazione del componente, viene descritta la progettazione di una possibile implementazione della catena elettronica necessaria per il funzionamento del buncher, inclusa la generazione e l'amplificazione del segnale elettronico e l'adattamento di impedenza con il dispositivo.

In conclusione, il presente lavoro studia la dinamica del fascio nella linea di iniezione e nella regione centrale del ciclotrone SPES. Per ottimizzare l'efficienza di iniezione, è stato progettato un dispositivo buncher, le cui prestazioni sono state stimate mediante simulazioni numeriche. Viene infine proposta una possibile realizzazione dell'elettronica necessaria al suo funzionamento.

CONTENTS

0 Introduction 1
- 0.1 SPES project at Legnaro National Laboratories 2
- 0.2 The cyclotron and its injection system 3
- 0.3 The buncher device 5
- 0.4 Software tools 8
  - 0.4.1 Simion 8
  - 0.4.2 Other physics simulators 9
  - 0.4.3 Post-processing tools 9

I Study of the cyclotron injection system

1 The injection line 13
- 1.1 The ion source 13
- 1.2 Transverse beam emittance 15
  - 1.2.1 Normalized emittance 18
  - 1.2.2 Ion source beam 20
- 1.3 The solenoids 20
- 1.4 The quadrupoles 23
- 1.5 The beam dynamics simulation 25
  - 1.5.1 The workbench and the Lua script 26
  - 1.5.2 Beam dynamics 27
- 1.6 Results 28

2 The cyclotron central region 31
- 2.1 The inflector 32
- 2.2 The magnetic field: bending and focusing 34
  - 2.2.1 The classical cyclotron 35
  - 2.2.2 The AVF cyclotron 38
- 2.3 The cavities and the electric field 40
- 2.4 The simulation workbench 42
- 2.5 Simulation results 43
  - 2.5.1 The longitudinal dynamics: energy and phase distribution. Phase acceptance. 45

2.5.2 Transmission and particle losses 47
2.5.3 The dee voltage amplitude 50
2.5.4 The phase difference 51

II Development of the buncher device

3 The buncher device 55
3.1 Advantages of introducing the buncher device 55
3.2 Description of the component and its working principle 56
3.2.1 Single gap buncher 56
3.2.2 Double gap buncher 59
3.2.3 Transit Time Factor (TTF) 60
3.3 Development of a buncher component 62
3.4 Results of particle dynamics simulations 65
3.4.1 Optimal operational parameters 66
3.4.2 Evaluation of injection efficiency improvement 66
3.4.3 Space charge effects and degradation of bunching efficiency 67
3.5 Other buncher designs and choice of the best configuration 70
4 The buncher electronics 75
4.1 Signal specifications and system building blocks 75
4.2 Signal conditioning 76
4.2.1 Phase Locked Loop 77
4.2.2 Variable attenuator 80
4.3 Signal amplification 83
4.4 The impedance matching circuit 84
4.4.1 Principles of impedance matching, transmission lines and Smith chart 84
4.4.2 The buncher matching network 88
5 Conclusions 95

Bibliography 99

0 INTRODUCTION

A very brief overview of SPES project is necessary to introduce the present work. The cyclotron and its main characteristics are presented before going to the main goal of the thesis: the study of the injection system and the central region of the cyclotron and the development of the buncher device.

A quick summary of the chapters follows:

1. The injection line and its components are discussed in the first chapter: the ion source, the solenoids, the quadrupoles. Some necessary beam dynamics concepts are reviewed and the principles of operation of each component are treated. The simulation of the beam transport through the injection line is presented.

2. The central region of the cyclotron is discussed in the second chapter. The principles of operation of each part are reviewed: the inflector, the radio frequency cavities, the magnetic field. The simulation of beam dynamics is presented and a comparison with the experimental data, collected during cyclotron operation, is addressed.

3. The third chapter introduces the buncher device. Its principles of operation are studied and the simulation of beam dynamics is presented, also accounting for space charge effects. Finally, a comparison among three similar buncher structures is addressed to evaluate the most convenient.

4. A purpose of electronics chain for the future realization of the buncher device is presented in the last chapter. The choice of components needed for signal conditioning, amplification and impedance matching is discussed.

The first two chapters form the first part of the thesis, where the existing system is studied and simulated and the simulations are compared with the experimental data. The last two chapters form the second part,

where the buncher device is studied and simulated and its future practical implementation is proposed.

0.1 SPES PROJECT AT LEGNARO NATIONAL LABORATORIES

SPES is the acronym of "Selective Production of Radioactive Species" and it is the first facility of its kind in Italy dedicated to nuclear physics and its applications [1].

At the moment, the SPES project is developing towards two leading scopes, among the four initial phases:

1. The production of radioactive exotic beams for research in fundamental nuclear physics.
2. The research on radioisotopes of interest for nuclear medicine, both for therapy and diagnostics.

The project exhibits a challenging complexity both as a whole and in each part of it. A plan of the facility is depicted in Figure 1. The core of the facility is the cyclotron that can provide two proton beams with energy ranging from 35 to 70 MeV and maximum combined current intensity of 750 μA. They are extracted from the two sides of the machine and transported by two main beamlines to the target rooms.

The target/ion source complex is dedicated to the production of exotic species with the ISOL ("Isotope Separation On Line") method. Receiving as input the primary proton beam from the cyclotron, it will produce a wide range of isotopes by fission of uranium carbide. At the moment, a silicon carbide target is used for testing the facility and for preliminary experiments.

Furthermore, the isotopes will be selected by means of the HRMS ("High Resolution Mass Separator"), enhanced in their charge state by means of the CB-MRMS ("Charge Breeder"-"Medium Resolution Mass Separator") and finally injected, through the Radio Frequency Qaudrupole, into the superconducting linac ALPI as a radioactive ion beam.

The nuclei chart in Figure 2 shows the expected re-accelerated exotic beams which can be obtained from the uranium carbide target. The radioactive ion beams will be available in the experimental rooms for the

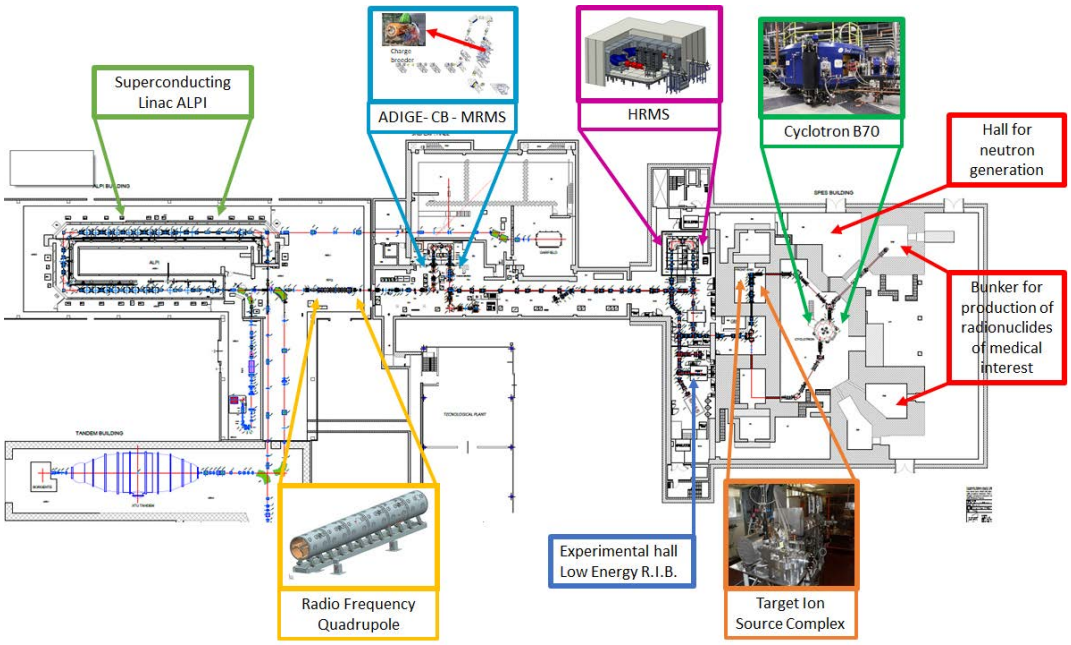

Figure 1: The plan of SPES facility as reported on the official website https://www.lnl.infn.it/spes/ .

nuclear physics experiments. Before re-acceleration an experimental room is dedicated to low energy experiments.

The research on radioisotopes of interest for nuclear medicine is the scope of LARAMED[1] and ISOLPHARM[2] projects [2]. Their aim is to search for radioactive species of interest for nuclear medical applications, both therapy and diagnosis. LARAMED employs the nuclear reactions triggered by the primary proton beam impinging on targets of several possible materials, such as Vanadium or Zinc. ISOLPHARM uses the nuclei among those available from the ISOL target station.

0.2 THE CYCLOTRON AND ITS INJECTION SYSTEM

The cyclotron employed in SPES project (Figure 3) is supplied by Best Theratronics. It is an Azimuthally Varying Field isochronous cyclotron, a

1 https://web.infn.it/LARAMED/
2 https://www.lnl.infn.it/isolpharm/

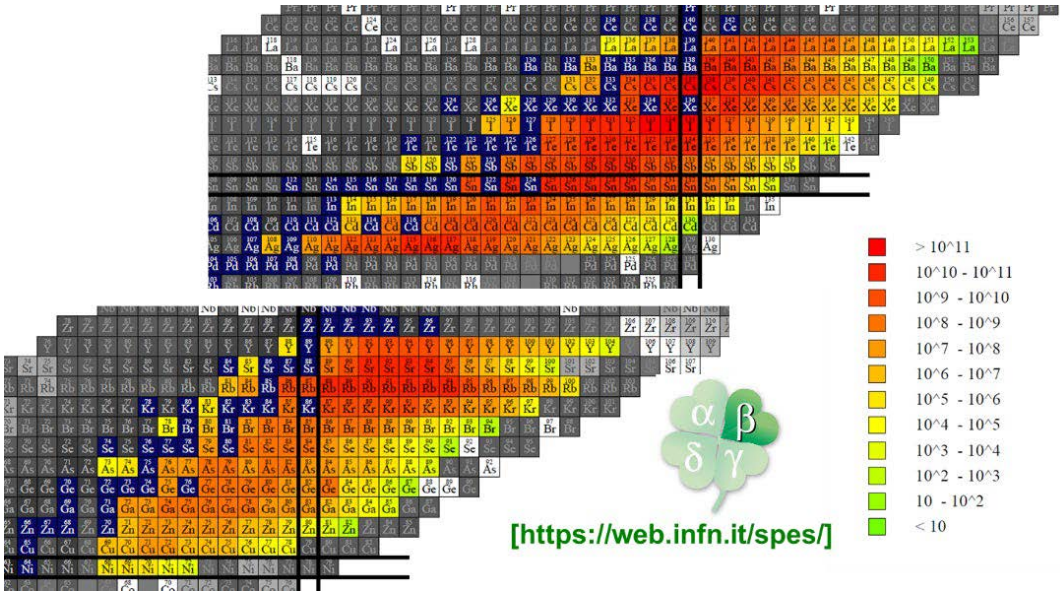

Figure 2: The expected reaccelerated radioactive beams producible with the uranium carbide target. The color map indicates the expected intensities as number of particles per second. Taken from [1].

compact machine which accelerates H^- ions and provides two proton beams extracted by means of two stripping carbon foils.

The ions come from a multi-cusp ion source with a low kinetic energy of $40\,keV$ and they are transported through the injection line upward to the cyclotron entrance. The injection line is composed of several magnetostatic elements: two solenoids and two quadrupoles for beam focusing, plus two steerers for little trajectory corrections. There is an empty vacuum chamber between the solenoids, where an optional component can be placed.

At the end of the injection line, above a collimator, the electrostatic spiral inflector bends the beam towards the median plane of the cyclotron, where acceleration is achieved by means of two radiofrequency cavities, called the *dees*[3]. Four accelerating gaps are located between the cavity edges and the grounded electrode. The magnetic field, that is necessary to bend the beam during the whole acceleration, is generated by the constant electric current flowing into two water-cooled coils at ambient temperature. The

3 This term is historically due to the cavity shape of the first cyclotron prototype, which resembled the "D" letter.

Figure 3: Picture of the cyclotron in its room at the SPES building.

particular shape of the iron poles creates the so-called "hills" and "valleys" of magnetic field. Thanks to them, an azimuthal component of the field comes up that is needed for vertical beam focusing during the second part of beam acceleration, when relativistic effects are not negligible. This is indeed the peculiarity of this kind of cyclotron.

One of the key characteristics of a cyclotron is its phase (or time) acceptance interval. Due to the fact that the accelerating field is not static, but oscillating, only a portion of the injected particles is selected for full acceleration, while the largest fraction of them is lost in the machine during the first turns, much earlier than reaching the extraction point. Actually, only one tenth of the particles produced by the ion source are effectively accelerated and extracted from the cyclotron.

The principal characteristics of the cyclotron of SPES project are summarized in Table 1.

0.3 THE BUNCHER DEVICE

The aim of the present work is to introduce the design of a buncher device for the SPES cyclotron to be installed in the injection line. Such device is needed for improving the injection efficiency of the whole system. As it will

Diameter	4.5 m
Type	Azimuthally Varying Field with 4 sectors
Particles	H^- ions / protons extracted
Beam extraction	Double extraction by stripping process
Energy range	From 35 MeV to 70 MeV
Current intensity	750 μA maximum
Magnetic field	1.6 T maximum
Radiofrequency	56.16 MHz (4^{th} harmonic)
Dee voltage amplitude	61 kV maximum
Phase acceptance	60 deg maximum
Ion source type	External multi-cusp
Source beam energy	40 keV
Source beam current intensity	8 mA maximum

Table 1: Summary of the cyclotron characteristics and operational parameters.

be pointed out, almost twice the actual beam current could be accepted by the cyclotron. Several benefits follows:

- It increases the beam current extracted from the cyclotron using the same input beam current coming from the ion source.
- It reduces the beam current needed from the ion source for the same beam current extracted from the cyclotron, reducing the degradation of the ion source.
- Less particles are lost in the machine, reducing the degradation of surfaces in the long term.

The buncher acts like a longitudinal lens, it compresses the continuous beam coming from the ion source into bunches, whose duration should be within the phase acceptance of the cyclotron. Achieving this can be done by means of a longitudinal force exerted on the beam particles by an electric field oscillating with the same frequency as the cyclotron cavities. A usual buncher mechanical structure is that of three coaxial copper tubular

electrodes placed along the beamline, forming two accelerating gaps, like a tiny Wideroe linac. The central electrode is driven by an oscillating electric potential while the other tubes are connected to ground. Two parameters have to be taken into account for buncher operation: amplitude and phase of the electric oscillating potential.

- The amplitude of the electric potential determines the focusing point where particles are bunched in a group.
- The phase of the electric potential oscillation have to be arranged with respect to that of the cyclotron cavities so that the bunches arrives at the right moment to be caught and accelerated by the cyclotron.

Moreover, an original possible implementation of the buncher device is proposed and discussed at the end of Chapter 3. It makes use of five electrodes instead of only three, having a total of four accelerating gaps. From the dynamics point of view the simulations show that its behavior is indistinguishable from those of the traditional two gap structures, but the needed voltage amplitude is the half. This translates into a less demanding radiofrequency system needed to operate the component.

The radiofrequency electronic chain that will be necessary to make the buncher device work properly has to manage the two signal parameters: the phase and the amplitude. Firstly, the signal conditioning block must generate a twin of the cyclotron signal locked to the same frequency and constant phase that should be also finely adjustable within a interval of some tenths of degrees to find experimentally the optimal value. For this scope a Phase Locked Loop circuit is the recommended choice. A practical realization of this circuit is proposed in Chapter 4 showing that the desired specifications can be achieved. The regulation of the signal amplitude is then easily obtained employing a voltage variable attenuator. The amplification of the signal will be addressed by a high power amplifier that has to be matched with the buncher device through an impedance matching circuit. The buncher device represents indeed a pure capacitive load that would reflect back all the power sent to it from the amplifier side and also the signal voltage amplitude would not reach the desired level on the buncher electrodes. An impedance matching block is then necessary both to prevent power being lost into the amplifier itself and to transform power into the

desired voltage on the buncher electrodes. The design of such a circuit involves the theory of transmission lines and is discussed in Chapter 4 as well.

0.4 SOFTWARE TOOLS

Several software tools will be used throughout the thesis. A brief summary of them follows.

0.4.1 *Simion*

The main software used for electromagnetic field computation and beam dynamics is Simion[4].

Simion is a general purpose software for ion tracking in electromagnetic fields in quasi-static approximation [3]. It employs finite difference methods for the computation of electric and magnetic fields by solution of Laplace equation and Runge-Kutta method for the ion trajectory computation. The software has a graphical user interface that allows the user to control the workflow of the simulation from the geometry of the system to the computation of fields and particle dynamics. In addition, Simion embeds a Lua[5] programming language interpreter and a Lua script can be run when launching a simulation. Many more features are available only using that script, such as importing and creating field maps, setting time-varying fields, exporting data in custom format for better post-processing, controlling the workflow of the simulation by creating branches and loops, among others.

Simion already provides the required capabilities for the analysis carried out in this work and our permanent Simion license allows unrestricted use of it, whereas the use of other software suites is restricted to specific necessary cases due to the limited number of licenses available at our institute.

4 https://simion.com/
5 https://www.lua.org/

0.4.2 *Other physics simulators*

Occasionally, other software tools have been used for the electromagnetic field computation: Opera[6] and Comsol[7].

The original model of the cyclotron was developed in Opera. It was used to compute the magnetic field map of the central region of the cyclotron that is necessary for running the beam dynamics simulations with Simion. Opera is a powerful finite element analysis software suite that allows very realistic electromagnetic field computations by solving Maxwell equations in materials. It was possible to simulate the magnetic field in the cyclotron iron poles due to the coil currents and in the vacuum space between poles where ions move. This physically accurate model cannot be obtained with Simion.

Comsol is another finite element analysis software devoted to multi-physics simulations. It was used for estimating the optimal gap length for the buncher design in Chapter 3 employing its parametric solution feature that allows automatically repeated computation of fields by sweeping a geometric design parameter.

0.4.3 *Post-processing tools*

For the visualization and manipulation of field maps two main tools were used: Python and Paraview.

Python[8] was the favorite choice for data analysis and manipulation of data to be adapted from one software to another one. Very often some simple operations on numeric tables were necessary like rearranging data in different formats, conversions between different measure systems.

Paraview[9] was preferred mostly for 3-dimensional field map visualization. It offers an interactive environment and makes it easy to process data and draw any kind of plot with only a graphic interface.

6 https://www.3ds.com/it/products/simulia/opera
7 https://www.comsol.it/
8 https://www.python.org/
9 https://www.paraview.org/

Part I

STUDY OF THE CYCLOTRON INJECTION SYSTEM

The injection system and the central region of the cyclotron are studied and analyzed in each part. Beam dynamics simulations are performed and compared with experimental data.

1

THE INJECTION LINE

The injection line is necessary to transport the beam from the ion source to the cyclotron entrance and to control its transverse characteristics for optimizing injection efficiency.

It is located under the cyclotron in a dedicated pit and is composed of four main magnetostatic components: two solenoids and two quadrupoles, plus two steerer magnets for beam alignment corrections, one located at the exit of the ion source and the other at the entrance of the second solenoid. The injection line is reproduced in Figure 1.1 where the main elements are represented with their location expressed in mm. The origin is where beam emittance was measured and it represents the starting point for the beam dynamics simulation. The location where the buncher device will be installed is also indicated.

The chapter discusses the working principle of each element of the injection line and introduces the key concepts of beam dynamics and the beam emittance. In the last part, the particle dynamics simulation of the injection line is presented with its results.

1.1 THE ION SOURCE

The ion source is of the multi-cusp volume-production type. A quick overview of this and other kinds of ion sources can be found in [4].

It is composed of a hollow cylindrical cavity, where hydrogen gas is injected and it becomes ionized, going to plasma state. The hydrogen plasma is triggered and sustained by the continuous arc discharge of a hot filament emitting electrons by thermionic process. In our case, discharge current is in the order of 100 A. The plasma is confined by the magnetic field produced by several permanent magnets placed all around the chamber with alternating polarity preventing the plasma from touching the surface.

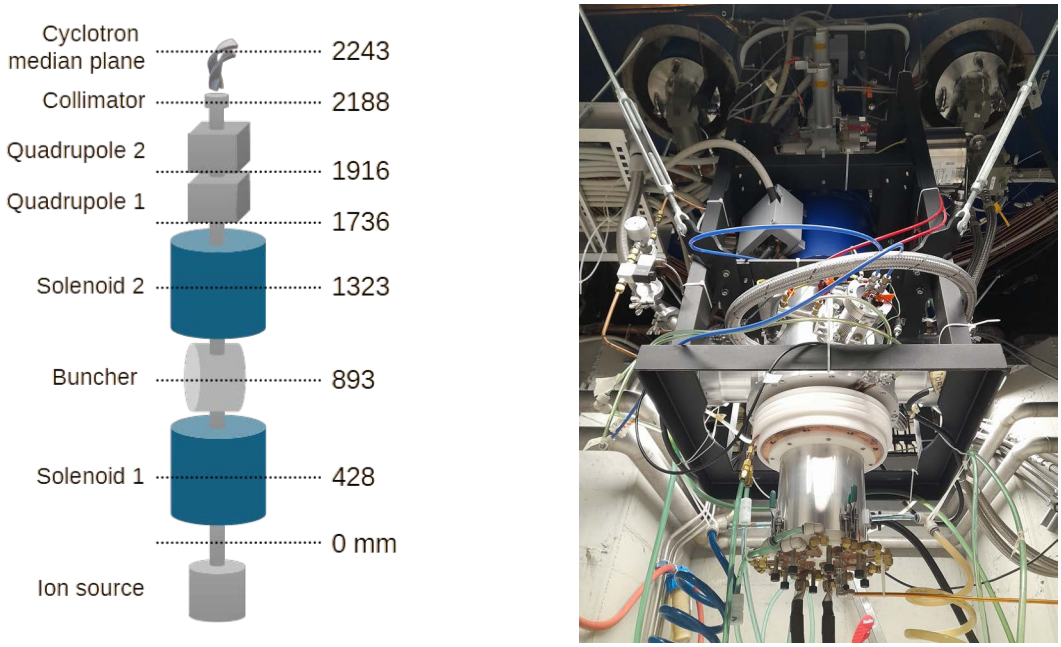

Figure 1.1: Illustrative drawing of the injection line with the position of the elements and picture of the real system. The ion source is at the bottom, the cyclotron median plane being on top. The distances from the origin are expressed in mm.

A dipole magnetic field, placed near the extraction hole, separates the plasma into two regions: a high temperature region where high energy electrons generate the plasma close to the filament and a low temperature region which only low energy electrons can reach by diffusion. In this second part of plasma, the volume production of H^- ions occurs by the process of dissociative attachment of low energy electrons (kinetic energy $\leq 1\,eV$) to vibrationally excited hydrogen molecules H_2^*:

$$H_2^* + e^- \rightarrow H^- + H^0 \tag{1.1}$$

The hydrogen molecules are excited by inelastic collisions with electrons in the first part of the plasma.

The extraction occurs by means of electrostatic lenses. In our case, the plasma chamber is connected to a $40\,kV$ power supply which ensures the beam being extracted at the energy of $40\,keV$. Several permanent magnets are placed at the exit of the plasma chamber between the extraction lenses and produce another dipole field to filter out the electrons extracted along with the H^- ions.

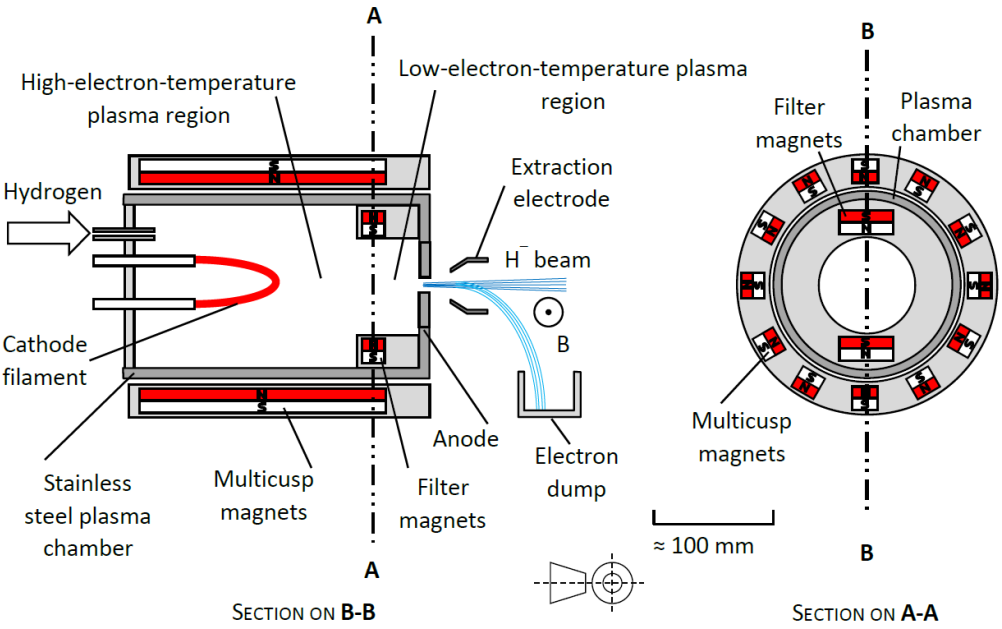

Figure 1.2: Schematic of a multi-cusp H^- ion source. Adapted from [4]

.

1.2 TRANSVERSE BEAM EMITTANCE

The ion source provides a continuous flux of ions exiting from the extraction hole with a certain velocity along the main axis and some transverse components.

In the most general case, a beam is represented as an ensemble of a certain number of particles whose dynamic state is defined at every time instant by their coordinates (x, y, z) and velocity components (v_x, v_y, v_z). It means that if we froze the beam at a certain time instant, it would be depicted as a cloud of points in the 6-dimensional space of the dynamic state variables, which is usually called phase space. The latter can be always split into three projections, or sub-spaces: (x, v_x), (y, v_y), (z, v_z).

Once specified the dynamic state of the ensemble at a fixed time instant and the force field which the particles are subjected to, the time evolution of the beam is determined by the solution of the equations of motion in the preferred formalism.

In our case, the beam transverse distribution and current are constant in time and particles forms indeed a steady flow having a main direction of

motion, let say z. It means that one of the velocity components, v_z, is much bigger than the other two. Based on this assumption, we can think the beam propagation in terms of longitudinal motion along z and transverse motions along x and y directions. As long as no quantities vary with time, we can use the z coordinate instead of time as parameter for the dynamic evolution of the beam. This choice is particularly useful when dealing with divergence angles instead of transverse velocity components, so we define

$$x' = \frac{dx}{dz} = \frac{v_x}{v_z} \qquad\qquad y' = \frac{dy}{dz} = \frac{v_y}{v_z} \tag{1.2}$$

The sub-spaces (x, x') and (y, y') are know as trace spaces. Using this point of view, we treat ion beams similarly to light rays in geometrical optics.

Transverse emittance is the key quantity summarizing the characteristics of the particle ensemble in terms of spatial extent and divergence/convergence. It is defined in each of the two transverse trace spaces (x, x'), (y, y') as the area, divided by π, of the ellipse containing a certain fraction of all the points in that space and it is usually measured as a length times an angle in $mm \cdot mrad$. Sometimes it is defined directly as the area of the ellipse and measured in $\pi \cdot mm \cdot mrad$, moving the π from the definition into the measurement unit. Emittance is usually indicated by the greek letter ϵ with a subscript referred to the transverse direction x or y.

From a statistical perspective, the point density distribution in each sub-space can often be approximated to a 2-dimensional Gaussian distribution. If we set in the space (x, x'), the density function looks like:[1]

$$f(x, x')) = \frac{1}{2\pi\sqrt{\det \boldsymbol{\Sigma}_x}} \exp\left\{ -\frac{\sigma_{x'}^2 x^2 - 2\sigma_{xx'} xx' + \sigma_x^2 x'}{2 \det \boldsymbol{\Sigma}_x} \right\} \tag{1.3}$$

where we have assumed that the mean values of x and x' are both zero so that the point distribution is centered in the origin of the reference frame.

1 As can be derived from the general expression of a n-dimensional Gaussian function [5] $f(\mathbf{x}) = \frac{1}{\sqrt{(2\pi)^n \det \boldsymbol{\Sigma}_x}} \exp\left\{ -\frac{1}{2}(\mathbf{x} - \boldsymbol{\mu}_x)^T \boldsymbol{\Sigma}_x^{-1} (\mathbf{x} - \boldsymbol{\mu}_x) \right\}$ where n is the number of dimensions, $\mathbf{x} = \begin{pmatrix} x \\ x' \end{pmatrix}$ and $\boldsymbol{\mu}_x = \begin{pmatrix} \mu_x \\ \mu_{x'} \end{pmatrix}$ are column vectors representing the particle coordinate x and divergence x' and their mean values μ_x and $\mu_{x'}$, $\boldsymbol{\Sigma}_x$ is the covariance matrix.

The covariance matrix $\mathbf{\Sigma}_x = \begin{pmatrix} \sigma_x^2 & \sigma_{xx'} \\ \sigma_{xx'} & \sigma_{x'}^2 \end{pmatrix}$ contains the variance [2] of each variable and their covariance, giving information about the spread of each variable and the coupling between them. Those are in fact the only three parameters needed to completely define the density function.

The emittance ellipse equation in the space (x, x') can be obtained just by intercepting the Gaussian surface with a horizontal plane where the amplitude of the Gaussian is reduced by the factor $e^{\frac{1}{2}}$:

$$\sigma_{x'}^2 x^2 - 2\sigma_{xx'} xx' + \sigma_x^2 x' = \det \mathbf{\Sigma}_x \tag{1.4}$$

It can be verified that the so-defined emittance ellipse contains the 39.35% of all the points in the trace space (x, x'). Indeed, using statistical terminology, the emittance ellipse is nothing else than the confidence ellipse of the 2-dimensional Gaussian distribution relative to a certain confidence probability that is the expected fraction of points contained in the ellipse. The concept of confidence ellipse is a generalization of confidence interval usually defined for a 1-dimensional probability distribution and can be extended to higher-dimensional distributions.

We can define the emittance ellipse for other values of the probability of particles falling inside the ellipse:

$$\sigma_{x'}^2 x^2 - 2\sigma_{xx'} xx' + \sigma_x^2 x' = k^2 \det \mathbf{\Sigma}_x \tag{1.5}$$

introducing the parameter k. The emittance ellipse results now from the interception between the Gaussian surface and a horizontal plane at the level where the amplitude of the Gaussian is reduced by factor $e^{k^2/2}$. This leads to the formula which can be used to calculate the probability p of particles falling inside the ellipse from the parameter k, as reported in [5]:

$$p(k) = 1 - e^{-k^2/2} \tag{1.6}$$

The meaning of the parameter k is the number of standard deviations taken by the ellipse in the directions of x and x', as it is shown in figure 1.3. Any value of k accounts for a different value of the probability of particles within the ellipse as listed in table 1.1.

2 The symbol of variance σ_x^2 helps to remind that it is the square of standard deviation σ_x.

From considerations about the emittance ellipse, as can be found in [6], it turns out that beam emittance is the square root of the determinant of the covariance matrix:

$$\epsilon_x = \sqrt{\det \boldsymbol{\Sigma}_x} = \sqrt{\sigma_x^2 \sigma_{x'}^2 - \sigma_{xx'}^2} \tag{1.7}$$

This equivalent definition leads to an easy generalization of emittance to 4 or 6 dimensions.

The emittance ellipse in the space (x, x') is usually re-written in the equivalent form:

$$\gamma_x \, x^2 + \beta_x \, x'^2 + 2\alpha_x \, x \, x' = k^2 \epsilon_x \tag{1.8}$$

where the so-called Twiss parameters substitute the elements of the covariance matrix:

$$\gamma_x = \frac{\sigma_{x'}^2}{\epsilon_x}, \qquad \beta_x = \frac{\sigma_x^2}{\epsilon_x}, \qquad \alpha_x = -\frac{\sigma_{xx'}}{\epsilon_x} \tag{1.9}$$

They are intended as the covariance matrix elements normalized over emittance.

Once the emittance of a beam is specified, the following relation, derived from (1.7), links together the Twiss parameters:

$$\gamma_x \beta_x - \alpha_x^2 = 1 \tag{1.10}$$

1.2.1 *Normalized emittance*

When a beam is accelerated in a specific direction, its transverse emittance naturally reduces because the longitudinal component of velocity increases by orders of magnitude compared with transverse components remaining the same as before acceleration.

For comparing transverse beam emittances at different energies is thus necessary to multiply the emittance by a normalization factor that cancels out the energy dependence of the emittance. The so-called normalized emittance is then a quantity defined as:

$$\epsilon_x^n = \beta \gamma \epsilon_x \tag{1.11}$$

where $\beta = v_z / c$ and $\gamma = 1/\sqrt{1 - \beta^2}$ are the usual relativistic quantities.

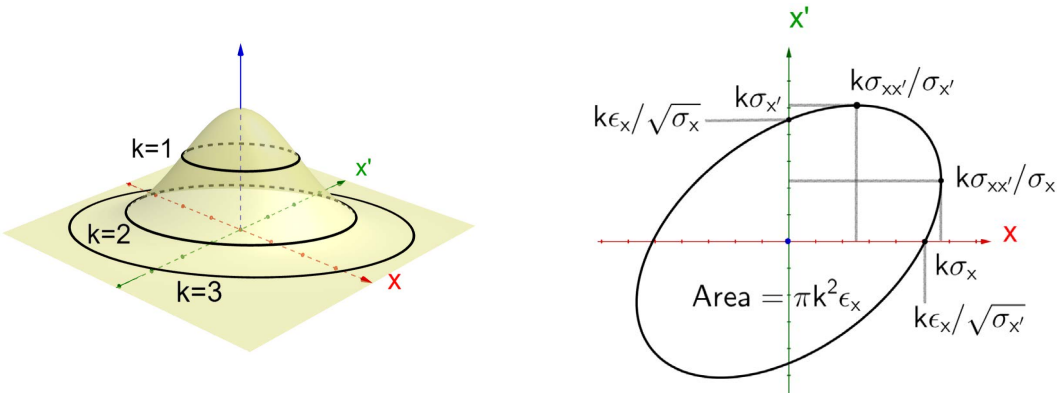

Figure 1.3: On the left, emittance ellipses of the 2-dimensional Gaussian distribution of the beam particles for different numbers of standard deviations $k = 1, 2, 3$. Summary of the emittance ellipse properties for a generic value of k. Images obtained with GeoGebra Calculator Suite.

Number k of standard deviations	Probability of particles within ellipse (%)
1	39.35
2	86.47
3	98.89
4	99.97
1.7941	80.0
1.9479	85.0
2.1460	90.0
2.4477	95.0

Table 1.1: Probability of particles falling inside the emittance ellipse corresponding to different values of the number of standard deviations k for the 2-dimensional Gaussian distribution. Adapted from [5].

	$u = x$	$u = y$
σ_u^2	42.418	56.987
$\sigma_{uu'}$	208.867	243.471
$\sigma_{u'}^2$	1072.651	1102.666

Table 1.2: The covariance matrix elements of the ion source beam measured by Best Theratronics for 90% of particles falling in the emittance ellipse for both transverse sub-spaces. Adapted from [7].

1.2.2 *Ion source beam*

The beam extracted from the ion source is represented as a 2-dimensional Gaussian statistical sample of points in each trace space using the experimental data given by Best Theratronics in [7]. The measurements of beam parameters were performed by Best Theratronics with an Allison scanner [3] at a distance of 154 *mm* from the source exit.

The measured covariance matrix is given for 90% probability of particles falling in the emittance ellipse corresponding to a number of standard deviations of $k = 2.1460$, but the true covariance matrix, the one defined for $k = 1$, is required to reconstruct the 2-dimensional Gaussian probability distribution. It can be obtained dividing the measured parameters by k^2. By means of a python script, employing the function *random.multivariate_normal(...)* from *numpy* library, the statistical sample of points is easily generated and stored in a csv file with the proper format to be given as input for Simion, as will be pointed out in section 1.5.

1.3 THE SOLENOIDS

After the ion source, two solenoids are placed to focus the beam in both transverse directions. The focusing principle of a solenoid is now briefly discussed.

A solenoid is a coil (with a certain length L, radius R and number of windings N) enveloping the beam pipe and producing an axially symmetric static

3 The working principle of this diagnostic device is explained by its inventor in [8].

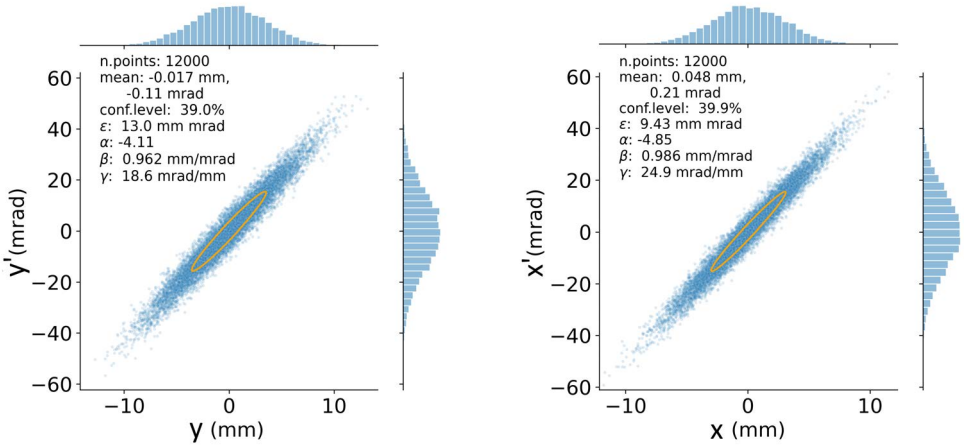

Figure 1.4: Transverse projections of beam phase space reconstructed as statistical samples from parameters measured by Best Theratronics.

magnetic field. The field components expressed in cyclidrical coordinates can be approximated to the first order terms. The axial component B_z can be considered uniform inside the solenoid while zero outside, depending only on the axial coordinate z. At the ends of the solenoid the field spreads out giving rise to a radial component B_r which is proportional to the radial coordinate r and to the first derivative of the axial component. The azimuthal component of the field is zero because of cylindrical symmetry. In formulas we can type:

$$B_z = B(z) \qquad B_\theta = 0 \qquad B_r = -\frac{r}{2}B'(z) \tag{1.12}$$

Figure 1.5 shows a plot of the solenoid magnetic field components (axial and radial) computed using the Biot-Savart solver embedded in Simion, as it will be explained.

A particle entering the solenoid exactly on its axis will not experience any force and passes through undisturbed. Let us consider, instead, a particle entering the solenoid with a direction parallel to the symmetry axis but with some transverse (radial) displacement. Its longitudinal component of velocity interacts with the radial component of the magnetic field giving to the particle an azimuthal kick and making it to rotate around the initial direction (not the solenoid symmetry axis). Because of this, when traveling through the central region of the solenoid, particle's velocity results to gain some radial component. When exiting from the solenoid an equal kick but in the opposite direction cancels the azimuthal component of velocity while the

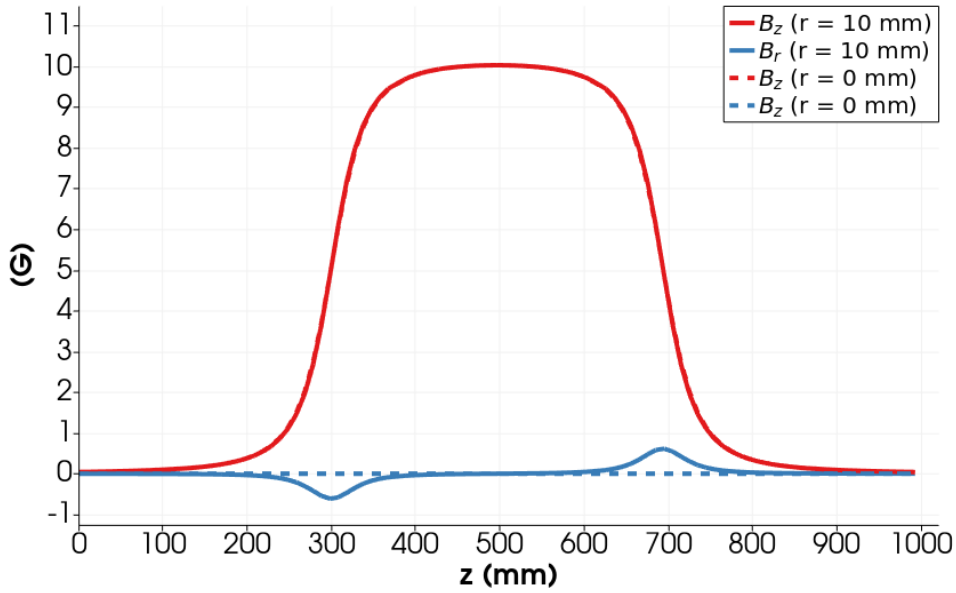

Figure 1.5: Solenoid magnetic field component. The axial and radial magnetic field components are represented as functions of the axial coordinate for different values of the radial coordinate.

radial component remains unchanged. This results in a beam being focused at one point far away from the solenoid exit with focal length f given by [9]:

$$\frac{1}{f} = \int_{-\infty}^{\infty} \frac{q^2 B^2}{4p^2} dz \tag{1.13}$$

where q is the ion electric charge, p its linear momentum and B the magnetic field strength.

In the hard-edge approximation of the solenoid the effective length can be defined as [10]:

$$L_{eff} = \frac{\int_{-\infty}^{\infty} B^2 dz}{B_{max}^2} \tag{1.14}$$

The magnetic field can be approximated with a couple of step functions in $z = 0$ and $z = L_{eff}$ and the focal length expression becomes:

$$\frac{1}{f} = \frac{q^2 B_{max}^2}{4p^2} L_{eff} \tag{1.15}$$

Both descriptions implicitly assume the thin lens approximation for the solenoid and the paraxial approximation for the beam. Those are valid in case of focus distance much larger than the solenoid length $f >> L$

and transverse displacement of ions much lower than the solenoid radius $x, y << R$.

When passing through the solenoid field the transverse dynamic variables x, x', y, y' become coupled with each other leading to a significant increase in the two transverse emittances. This coupling effect is particularly evident when the solenoids are represented as thin lenses using the matrix formalism. In that case, the phase space should not be split into two separate 2-dimensional sub-spaces, but the beam dynamics should be analyzed in the 4-dimensional transverse phase space to observe beam emittance conservation.

More details on charged particle dynamics in solenoids can be found in [9] and [11] as well as textbooks like [12] and [10].

Each solenoid of our injection line is formed by a coil enveloped by an iron shell. The coil itself is made by 8 layers of 40 windings each, for a total of 320 windings. Typical values of intensity of currents flowing in the wire during operation are in the order of hundreds of Ampére. A water circuit ensures heat dissipation.

1.4 THE QUADRUPOLES

Quadrupoles are the other focusing elements of the injection line.

Their geometrical structure is made of four iron poles with hyperbolic profile extruded along the beam axis for a certain length. The quadrupole aperture is the minimum distance a between the center and the pole surface. Each pole is magnetized by a coil with n number of windings and a certain electric current I flowing in it (see right side of Figure 1.6). The magnetic field resulting in the space between the four poles around the beam pipe has components expressed in the normal cartesian reference frame:

$$B_x = B'y \qquad B_y = B'x \qquad B_z = 0 \tag{1.16}$$

The two transverse components B_x and B_y scale linearly with the ion transverse coordinates y and x. The field gradient $B' = \partial B_x/\partial y = \partial B_y/\partial x$ is a constant which indicates how fast the field increases with the transverse displacement and it can be expressed in terms of the coil current as $B' = 2\mu_0 nI/a^2$. The axial component B_z is zero because of translation symmetry.

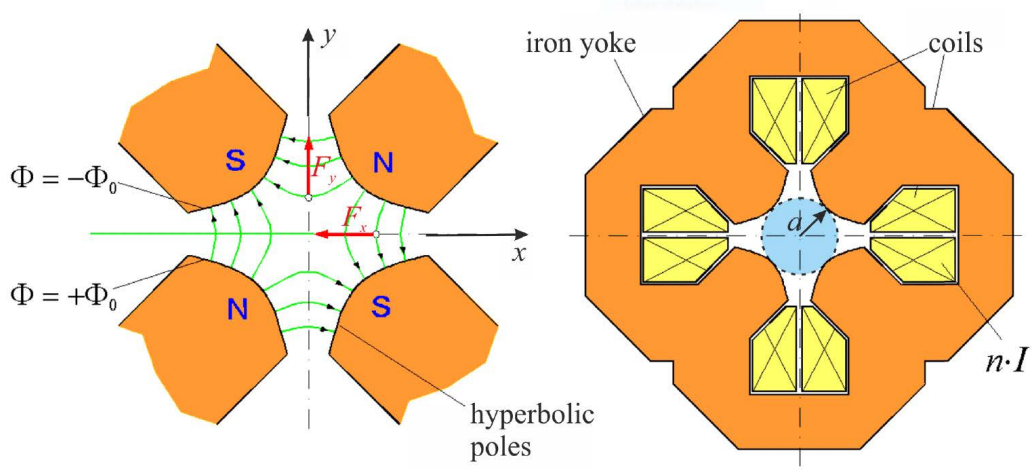

Figure 1.6: Illustration of quadrupole structure projected on the plane xy transverse to the beam direction. The magnetic field lines and the force vectors acting on the ions are represented on the left. Adapted from [6].

The quadrupole field can be obtained from the scalar potential function $\Phi(x,y) = B'xy$, as explained in [6], motivating the hyperbolic shape of the pole profile. Potentials at surfaces are equal to $\pm\Phi_0 = \pm B'a^2/2$.

Considering the force acting on ions traveling along the axial direction z with some x or y transverse displacements, a beam passing through the quadrupole results to be focused in the y direction, while de-focused in the x direction (look at left side of Figure 1.6). This explains why quadrupoles are required at least in doublets for having a net focusing action in both transverse directions. In the thin lens and paraxial approximation, the focus lengths of a quadrupole are given by:

$$\frac{1}{f_x} = -\frac{q}{p}B'L_{eff} \qquad \frac{1}{f_y} = \frac{q}{p}B'L_{eff} \tag{1.17}$$

the effective length being defined as:

$$L_{eff} = \frac{\int_{-\infty}^{\infty} Bdz}{B_{max}} \tag{1.18}$$

A quadrupole acts on each transverse direction independently so that no coupling is expected between the transverse dynamic variables of a beam passing through it. This is evident when looking at the matrix description of a quadrupole.

Element	Current (A)	Aperture (mm)	Length (mm)
Solenoid 1	234.0	42.5	392
Solenoid 2	173.0	42.5	392
Quadrupole 1	18.3	25	120
Quadrupole 2	42.0	25	120

Table 1.3: Optimal experimental parameters of the injection line elements and their geometric dimensions.

The injection line quadrupoles have an effective length of $120\,mm$. The field measured at the pole surface is $448\,G$ for an electric current of $46.5\,A$. The field gradient results to be:

$$B' = \frac{B}{a} = \frac{448}{25}\left[\frac{G}{mm}\right] = 17.92\left[\frac{G}{mm}\right] \tag{1.19}$$

given that the quadrupole aperture is $a = 25\,mm$. Finally, the field gradient B' at any other value of current I can be calculated using the proportion:

$$B'\left[\frac{G}{mm}\right] = I[A]\cdot\frac{17.92}{46.5}\left[\frac{G}{mm\cdot A}\right] = I[A]\cdot 0.3854\left[\frac{G}{mm\cdot A}\right] \tag{1.20}$$

1.5 THE BEAM DYNAMICS SIMULATION

The scope of the simulations presented in this chapter is to reproduce the actual beam in the injection line as a preliminary step for the simulation of the central region of the cyclotron (treated in chapter 2) and the simulations with the buncher device (in chapter 3).

All the main parts and concepts have been described in the preceding paragraphs. It is now time to discuss the the virtual environment where the simulation of beam dynamics is performed.

During the operation of the injection line the best parameter values were found to give the maximum beam transmission at the cyclotron extraction. They are reported in table 1.3.

As stated in the Paragraph 0.4 the software package preferred for the beam dynamics simulation is Simion [3].

1.5.1 *The workbench and the Lua script*

In the Simion code, the workbench represents the environment where any system can be simulated. The building blocks of every project are the so-called potential arrays that can be of two kinds: electric and magnetic, with planar or cylindrical symmetry. Each potential array contains the information about electrode geometries and the 3-dimensional map of electric or magnetic scalar potential given by the solution of Laplace equations [4]. Simion indeed only works with static fields. Time-varying fields can be simulated, but only in the quasi-static approximation (length of the system much shorter than wavelength of the fields).

Once the building blocks have been placed in their desired position in the virtual space of the workbench, particle tracking can be performed and particle information can be recorded at every time step of the simulation.

A key feature of Simion is the embedded Lua interpreter. Many aspects of the simulation are controlled only by running the Lua script during the simulation. A list of relevant functions includes:

- import external field maps from csv files;
- change the electrode potentials or the fields at every simulation time step;
- define time step duration;
- loop simulations over a parameter;
- write data to a csv file;

For the injection line a single magnetic potential array was employed with grid step size of 1 *mm*, length 2260 *mm*, height and width 100 *mm*.

The magnetic field of the solenoids was computed using the Simion Biot-Savart solver just by calling the *MField.solenoid_hoops(...)* [5] function from

4 In the Simion jargon solving the Laplace equations is referred to as "refining" the potential array.

5 The function requires as arguments: the electric current, the coordinates of the starting and ending point, the radius and the number of turns. A field-map-like object is returned that gives back the field components when called specifying the coordinates of the point where one wants to know the field.

the *simionx.MField* module. The solenoid structure is approximated with a single-layer coil made of 320 thin windings without any iron shield, solenoid length being 392 mm and radial aperture of 42.5 mm. This rough simplification, though, yielded reasonable results in the beam dynamics simulations. For reducing the computational effort required by the beam dynamics simulation, the solenoid field map was computed for the value of 1 A of current in a restricted volume, exported as a csv file with a resolution of 2 mm grid step size and finally re-imported in the injection line workbench and multiplied by the desired value of current. The solenoid field components resulting from Simion calculation are shown in Figure 1.5 for the reference value of 1 A of current giving a maximum axial magnetic field of about 10 G at the center of the solenoid.

The magnetic field map of the quadrupoles was defined as a *FieldArray* object directly using the formulas (1.16). The effective length of the quadrupoles is 120 mm and their aperture is 25 mm, as reported in [7]. The magnetic field gradient in the operational conditions was computed using the formula (1.20).

In the last part of the injection line the cyclotron field is present and should be taken into account for the simulation. As it will be pointed out in the next chapter 2, the field map was computed using Opera software package, exported in a csv file and imported as a *FieldArray* object into the Simion workbench. The 3-dimensional model of the cyclotron was indeed available, but Opera was avoided for particle dynamics simulations, being preferred only for the magnetic field computation.

1.5.2 *Beam dynamics*

When forces are applied to the particles, the evolution of the beam dynamics is obtained by the solution of the equation of motion. In our case we consider only electric or magnetic forces acting on the particles, neglecting any other physical effect. The Lorentz law gives the expression of those forces as function of the fields:

$$\vec{F} = q\vec{v} \times \vec{B} \tag{1.21}$$

The approximation of no space charge effects in the beam transport line can be explained by the phenomenon of space charge neutralization due to

residual gas ionization. Some molecules of hydrogen gas dispersed along the transport line can be ionized by the negative beam ions. Such positive ions accumulate in the negative beam potential well, electrons being repelled instead, and after a certain characteristic time their concentration reaches an equilibrium with the beam. This effect naturally occurs in negative ion transport lines depending on the residual gas pressure and can lead to almost complete space charge compensation [10] [13] [14]. This is indeed the case at the operating pressure of 10^{-7} *mbar* of our injection line, in agreement with results reported in the literature.

1.6 RESULTS

The first beam feature to observe is the beam envelope, defined as the standard deviation (assuming Gaussian distribution) of the transverse ion coordinates along the beam axis. In the left plot of figure 1.7 a sample of 500 out of the total number of 12000 ion trajectories is represented. Line transparency is used to highlight the local particle density inside the beam pipe: the overlap of many trajectories results in a color intensity proportional to the number of ions passing through a given region. Some trajectories terminate before reaching the final plane because they exceed the geometric aperture of the elements.

On the right side of Figure 1.7 the beam envelope is plotted for the two transverse directions using an expanded scale. In the reference frame of Simion workbench the x axis represents the longitudinal coordinate, while y and z axes denote the transverse coordinates. Although it may seem counter-intuitive, this choice satisfies the natural reference frame used in Simion to define particle initial variables.

The final distribution of points in the transverse sub-spaces is represented in Figure 1.8. In Table 1.4 the input and output emittances and Twiss parameters are reported for the starting plane at ion source exit and for the final plane located just before the collimator.

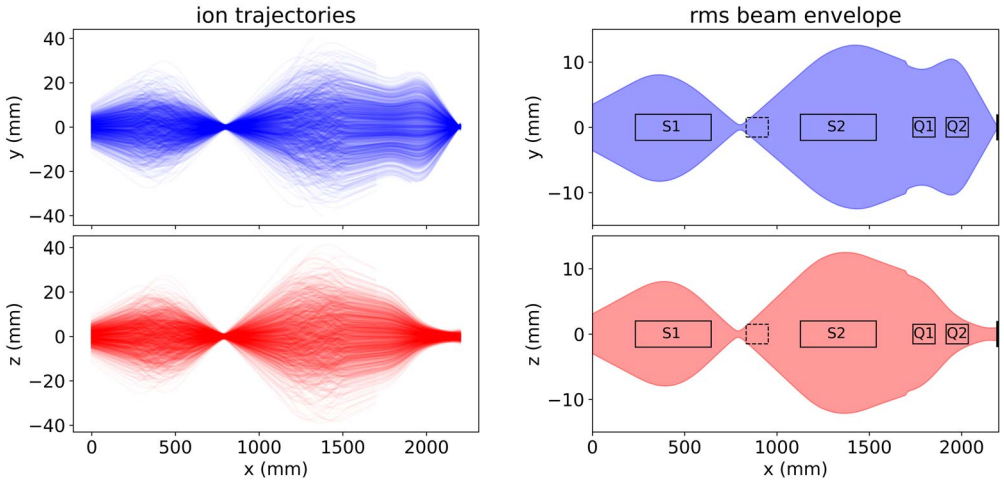

Figure 1.7: A sample of 500 ion trajectories resulting from the particle tracking simulation along the injection line. In the right plot the area occupied by the beam is represented as the root mean square (rms), or standard deviation, beam envelope.

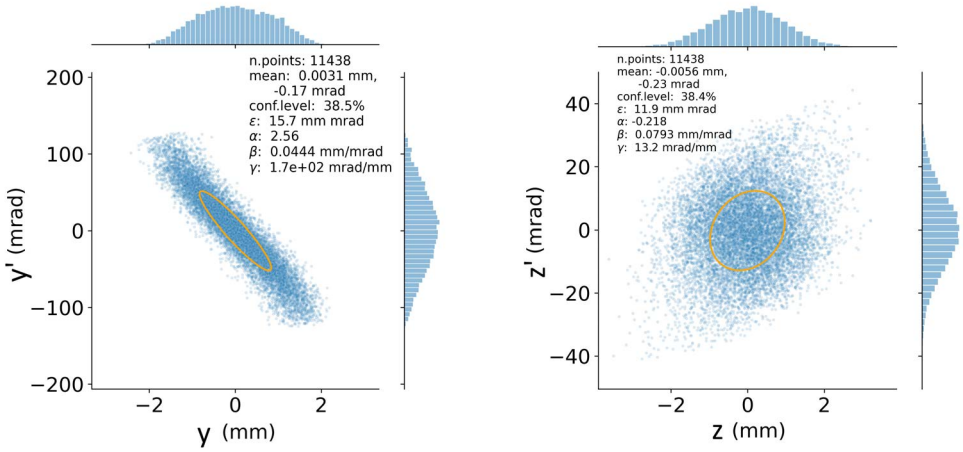

Figure 1.8: Point distributions in the two transverse sub-spaces at the end of the injection line, just before the collimator.

	At ion source exit ($x = 0\,mm$)	Before collimator ($x = 2179\,mm$)
ϵ_y, ϵ_z $(mm \cdot mrad)$	13.0, 9.43	15.7, 11.9
α_y, α_z	-4.11, -4.85	2.56, -0.218
β_y, β_z $(mm/mrad)$	0.962, 0.986	0.0444, 0.0793
γ_y, γ_z $(mrad/mm)$	18.6, 24.9	170, 13.2

Table 1.4: Emittance and Twiss parameters of the beam at the starting point and before collimator.

2

THE CYCLOTRON CENTRAL REGION

A quick overview of the SPES cyclotron characteristics was given in the introduction. In this chapter, the principles of cyclotron operation are treated in detail and the simulation workbench of the cyclotron central region is described.

The scope of this chapter is to utilize the results of the preceding one to simulate the particle dynamics in the cyclotron central region. The outcome of these simulations will be compared with the experimental data available during the operation of the machine in order to see how good the model approximates reality.

This will be the starting point of the following chapter for evaluating the performance of a new device to be installed in the injection line, the buncher, which is the final scope of the thesis.

Another purpose of our research team at Laboratori Nazionali di Legnaro is the realization of a chopper device, whose development was conducted in parallel with the buncher but it is not treated in the present work. This device is required for adapting the cyclotron proton beam to the specifications of the SPES target/source station. Details can be found in [15].

The simulations presented at the end of this chapter will focus on the longitudinal beam dynamics that involves the acceleration process and the phase acceptance of the machine. Previously, we dealt with a continuous flux of particles, describing how they move in the transverse direction. Now, the particle energy and time distribution will gain our attention and also particle losses inside the cyclotron central region will be studied.

Before discussing the simulation workbench and the results, the main functional blocks of the cyclotron are explained in the following paragraphs:

- The electrostatic spiral inflector injects in the cyclotron center the beam coming from the external ion source.
- The azimuthally variable magnetic field ensures beam transport through the machine.

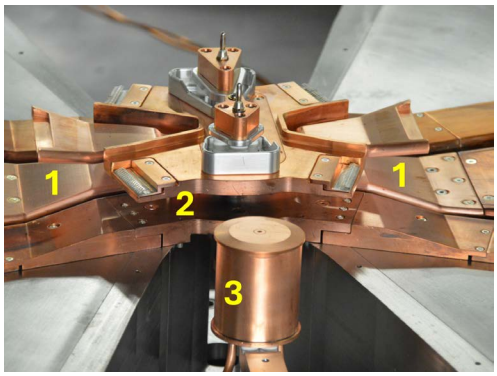

Figure 2.1: Picture of the central region of the SPES cyclotron. The yellow labels indicate: 1) the tips of the radiofrequency cavities, 2) the grounding electrode, 3) the pop-up probe.

- The accelerating structure increases particle kinetic energy to the designed value.

At the radius corresponding to the energy of about 1 MeV a movable Faraday cup (or pop-up probe) inside the machine can be remotely operated to stop the beam and measure its current. It is the copper cylinder visible in the foreground in Figure 2.1. This diagnostic instrument is necessary during machine operation to optimize the parameters of the injection line and the cyclotron before extracting the beam at full energy. It was also used for collecting the experimental data to be compared with the simulations of the central region.

2.1 THE INFLECTOR

The inflector is located at the cyclotron entrance after the collimator at the end of the injection line. It is composed of two metallic electrodes with a particular spiral shape whose aim is to bend the beam coming from the injection line towards the median plane of the cyclotron where the acceleration can be achieved.

To make this task reliable, an electric potential difference is applied across the couple of electrodes to create an electric field that is orthogonal to the beam trajectory at each point due to the particular spiral shape. This ensures that the beam is bent but its energy is not changed, because no components of the electric field point in the direction of motion of the particles. At the

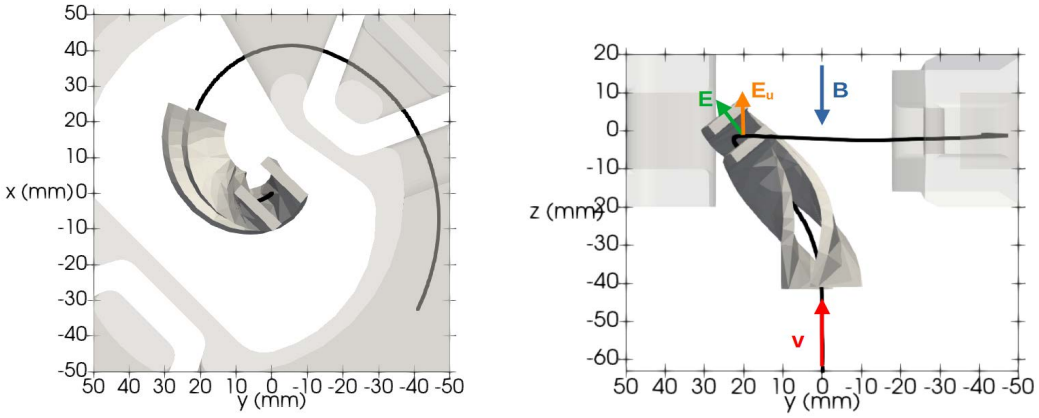

Figure 2.2: 3D model of the spiral inflector of SPES cyclotron in the central region with simulated single particle trajectory. Bottom and lateral views are shown.

same time the magnetic field generated by the main magnet of the cyclotron forces the particles to bend around the vertical axis.

The electrode geometry is designed so that the combined action of the electric and the magnetic fields produces the desired trajectory that matches the first orbit in the cyclotron.

The analytical parametric equations $x = x(b)$, $y = y(b)$, $z = z(b)$ of the central particle trajectory in the spiral inflector can be derived by solving the equations of motion of the particle with the assumptions of a uniform magnetic field B directed along the vertical z axis, a null component of the electric field along the velocity of the particle $E_v = 0$, and constant component E_u of the electric field in the direction $\hat{u}$ orthogonal to both the ion velocity $\vec{v} = v_x\hat{i} + v_y\hat{j} + v_z\hat{z}$ and the vector $\vec{h} = v_y\hat{i} - v_x\hat{j}$ lying on the xy plane (the cyclotron median plane). The trajectory of particles is determined by choosing the value of two design parameters, the electric bending radius A and the tilt parameter k', defined as follows:

$$A = \frac{mv_0^2}{qE_u} \tag{2.1}$$

where m, q and v_0 are the mass, the electric charge and the design speed of the ion, and

$$k' = \frac{\tan[\theta(b)]}{\sin[b]} \tag{2.2}$$

where $b \in [0, \pi/2]$ is the parameter of trajectory equations, related to time by $b = (v_0/A)t$, and $\theta(b)$ is the instantaneous angle between the direction $\hat{u}$ and the electric field vector $\vec{E}$. The tilt parameter k' at the inflector exit ($b = \pi/2$) corresponds to the value of the tangent of the electrode angle with respect to the vertical direction.

The extent of the spiral inflector in the vertical z direction is determined completely by the value of paramter A, while in the horizontal xy plane (the cyclotron median plane) it is determined by both parameters A and k'. More details about the inflector design can be found in [16] and [17].

Another aspect of the inflector design is that the beam transverse emittance ellipse at the output of inflector should match the cyclotron auto-ellipse at the injection orbit to avoid filamentation and consequent emittance growth in the following turns [23].

2.2 THE MAGNETIC FIELD: BENDING AND FOCUSING

The magnetic field of the cyclotron is necessary to bend the particle trajectories throughout the entire acceleration process, forcing them to pass repeatedly through the same accelerating gaps, until they reach the extraction point. Particles starts from the center of the machine and travel along spiral trajectories lying on the median plane between the poles of the main dipole magnet, being finally extracted at the periphery of the machine.

In the case of SPES cyclotron particles are injected from an external source by means of the spiral inflector and extracted by stripping process passing through a very thin carbon foil that removes the two electrons from the H^- ion. The resulting protons have opposite charge and their path is circular but with opposite curvature in the magnetic field so that they naturally go out of the machine as illustrated in the sketch of Figure 2.3.

Some literature items were particularly useful to learn the cyclotron working principles, starting from the historical book by Livingood [18] up to the more recent review [19], passing through the CERN Accelerator School lecture proceedings [20] [21] [22].

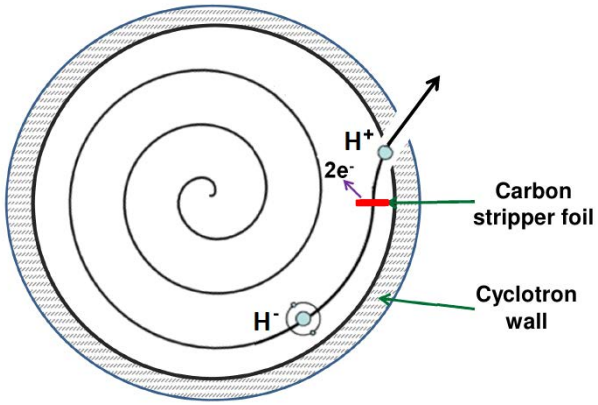

Figure 2.3: Sketch of single particle trajectory in a cyclotron and extraction by stripping process.

2.2.1 *The classical cyclotron*

In an ideal cyclotron the key condition for acceleration is set by the synchronism between the accelerating electric field and the revolution of particles in the magnetic field, also called the isochronous condition:

$$\omega_{RF} = h \cdot \omega_{rev} = h \cdot \frac{qB_z}{\gamma m_0} \tag{2.3}$$

where ω_{RF} is the frequency of the accelerating electric field, ω_{rev} is the revolution frequency of particles with relativistic factor γ, rest mass m_0 and charge q in the axial magnetic field B_z of the cyclotron and h is an natural integer called harmonic number. By defining the cyclotron frequency as $\omega_c = \frac{qB_z}{m_0}$, the revolution frequency is expressed as $\omega_{rev} = \omega_c/\gamma$.

In the non-relativistic domain ($\gamma \approx 1$), the isochronous condition is satisfied by a uniform axial magnetic field with value $B_{iso} = B_0 = \frac{m_0}{q}\omega_c$. The revolution frequency scales with the magnetic field approximately as $f_c = \frac{\omega_c}{2\pi} \approx 15.2\,[MHz] \cdot B_z[T]$ for protons, so that the frequency of the accelerating electric field usually stays in the domain of radio frequencies (tens/hundreds of MHz). In the case of SPES cyclotron $f_{RF} = 56.16\,MHz$ with harmonic number being $h = 4$.

At the same time, the magnetic field must ensure beam confinement in the transverse[1] directions of motion (radial and vertical) to achieve the beam transport along the accelerating path.

The mechanism of beam focusing in the classical cyclotron, like the first prototype by Lawrence, is reported in the literature as "weak focusing" because the field produces a weak action on the beam, focusing it continuously in both transverse directions throughout the entire accelerating path.

The magnetic field configuration in classical cyclotrons was produced simply by a dipole magnet with almost flat pole surfaces. The weak focusing was achieved by the axial and radial components of the magnetic field naturally occurring when the field decreases with radius.

To quantify the field gradient and set the condition for weak focusing, the field index k was defined as the ratio between relative axial field variation and relative radial variation:

$$k = \frac{dB_z / B_z}{dr / r} \tag{2.4}$$

In the first order approximation the transverse particle dynamics equations can be derived considering only the action of the static magnetic field (without any electric field), showing that two restoring forces, radial and axial, act independently on the particles like elastic forces proportional to the radial and axial displacement from the reference circular trajectory (orbit). In this simplified picture, the transverse motion of the particles in the beam results to be a combination of two independent harmonic oscillations along the axial and radial directions about the reference trajectory. The frequency of these oscillations is directly related to the strength of the restoring force. They are called betatron tunes [2] and are defined as the ratio between the frequency of betatron oscillation and revolution frequency of the reference orbit:

$$\nu_r = \frac{\omega_r}{\omega_{rev}} = \sqrt{1+k} \qquad \nu_z = \frac{\omega_z}{\omega_{rev}} = \sqrt{-k} \tag{2.5}$$

1 The cylindrical coordinates (z, r, θ) are the most natural for describing particle dynamics in the cyclotron. We refer to the vertical (or axial) z and the radial r as the transverse components of motion, and to the azimuthal θ as the longitudinal component.

2 Historically, this effect was studied in betatron accelerators.

From the above formulas, it follows that the range of field index that allows weak focusing, the so-called weak focusing condition, is:

$$-1 < k < 0 \tag{2.6}$$

Now, in a classical cyclotron, where the electric field frequency ω_{RF} is fixed, the isochronous condition (2.3) is in contrast with the weak focusing condition (2.6), that requires a radially decreasing magnetic field instead of a simply uniform field. The particles moving at a certain radius will be subjected to a field $B_z(r)$ different from the isochronous field B_{iso}, the one that satisfies the isochronous condition. In a single revolution the particles get a phase variation with respect to the radiofrequency (delay or advance, depending on the sign) equal to:

$$\Delta\phi = 2\pi \frac{\omega_{RF} - h\,\omega_{rev}}{\omega_{rev}} = 2\pi h \frac{B_z(r) - B_{iso}}{B_z(r)} \tag{2.7}$$

This phase change accumulates turn over turn and, when it reaches 180 deg, acceleration becomes impossible: particles start to be decelerated back to the center along an inverse path.

A strategy to mitigate this problem is setting the maximum value of magnetic field in the central region a bit higher than the isochronous field so that, while decreasing as required by (2.6), the isochronous condition is met only at one intermediate radius r_{iso} between injection and extraction where $B_z(r_{iso}) = B_{iso}$. This is illustrated in Figure 2.4. Two regions are recognizable: one where the field is higher and another when it is lower than the isochronous field. As a result, the particles will never be exactly in phase with the oscillating electric field, but the phase interval, where acceleration is achievable, is kept as large as possible.

Though effective, the weak focusing configuration poses limits on the reachable beam energies. When relativistic effects are not negligible anymore, acceleration cannot go further because particles start to loose synchronism with the accelerating field. The revolution frequency of relativistic particles decreases with the relativistic factor γ and the magnetic field should increase with radius to keep the synchronism:

$$B_{iso}(r) = B_0\gamma(r) = \frac{B_0}{\sqrt{1 - \left(\frac{\omega_c r}{c}\right)^2}} \tag{2.8}$$

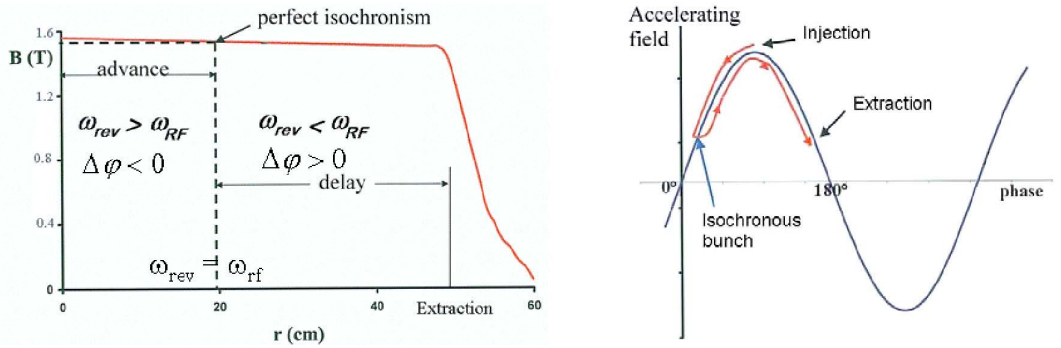

Figure 2.4: Illustration of the particle phase evolution in a classical cyclotron with $h = 1$. Adapted from [20].

requiring the field index to be $k = \gamma^2 - 1$.

As a result, the weak focusing remains possible in the radial direction but impossible to achieve in the vertical direction.

2.2.2 *The AVF cyclotron*

The solution to this problem came with the design of the Azimuthal Varying Field (abbreviated in AVF) cyclotron by L. H. Thomas. The idea is to create a field that varies in the radial direction as required to satisfy the isochronous condition, but also varies in the azimuthal direction forming alternate zones of higher and lower magnetic field, also called "hills" and "valleys". This creates an azimuthal component of the magnetic field at the edge between those regions. The curvature radius of particle trajectory also changes when passing from regions of different magnetic field and a radial component of the particle velocity appears. The resulting Lorentz force has always vertical direction and points towards the median plane, so that it exploits a focusing action when passing from hill to valley or valley to hill. The resulting effect is beam confinement in the vertical direction. In the case of SPES cyclotron there are four hills and four valleys.

The Figure 2.5 clarifies the focusing mechanism in AVF cyclotrons. The equilibrium orbit (4) deviates from a simple circumference (3). When passing through a hill (1) or a valley (2), the radius of curvature of the particle trajectory respectively reduces or increases causing a radial component of the velocity to appear. At the same time the magnetic field bulging from

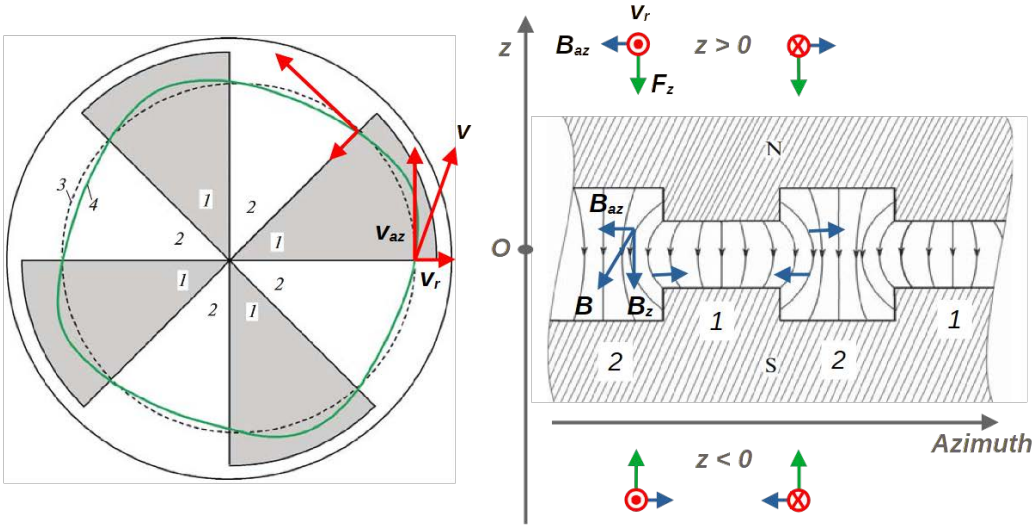

Figure 2.5: Illustration of vertical focusing in AVF cyclotrons. Adapted from [19].

hills to valleys exhibits an azimuthal component $\mathbf{B}_{az}$ when the displacement from the median plane is $z \neq 0$. The resulting axial force $\mathbf{F}_z = q\mathbf{v}_r \times \mathbf{B}_{az}$ is always directed towards the median plane ensuring a focusing action on the beam particles.

The focusing strength is directly proportional to the field variance between hills and valleys, the so-called flutter:

$$F = \frac{\langle B_z^2 \rangle - \langle B_z \rangle^2}{\langle B_z \rangle^2} \tag{2.9}$$

The betatron tunes for an AVF cyclotron take the approximate form:

$$\nu_r = \sqrt{1 + k} \qquad \nu_z = \sqrt{-k + F} \tag{2.10}$$

The radial profile of the magnetic field of an AVF cyclotron, like that of SPES cyclotron shown in Figure 2.6, usually has a first part where the flutter is almost null ($F = 0$) and the particles have still low kinetic energy just after the injection, so that the axial focusing is achieved by means of a negative field gradient, like in a classical weak focusing cyclotron. This action is exploited by a magnetic field bump in the central region ($r < 250\,mm$). When particles reach relativistic energies the magnetic field starts rising to keep the synchronous condition until the extraction point.

Another mechanism of focusing that occurs in the first few turns in the central region is due to the vertical component of the electric fields across

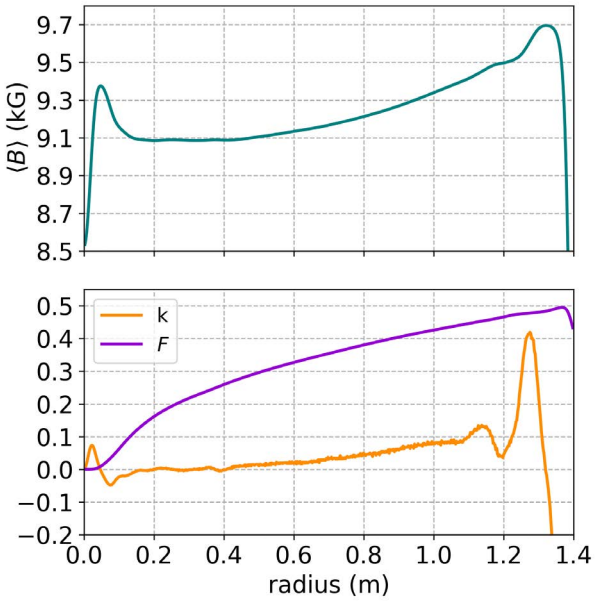

Figure 2.6: The full measured radial profile of the mean magnetic field $\langle B \rangle$ of SPES cyclotron with flutter F and field gradient k.

the accelerating gaps [23]. This effect is inversely proportional to the number of turns. It achieves the maximum when particles pass through the gap during the interval of falling voltage (see Figure 2.7).

2.3 THE CAVITIES AND THE ELECTRIC FIELD

In a cyclotron the accelerating system is composed by a certain number of electrodes named the "dees" because in the first classical cylotrons they resembled the shape of letter "D". The accelerating electric field is confined

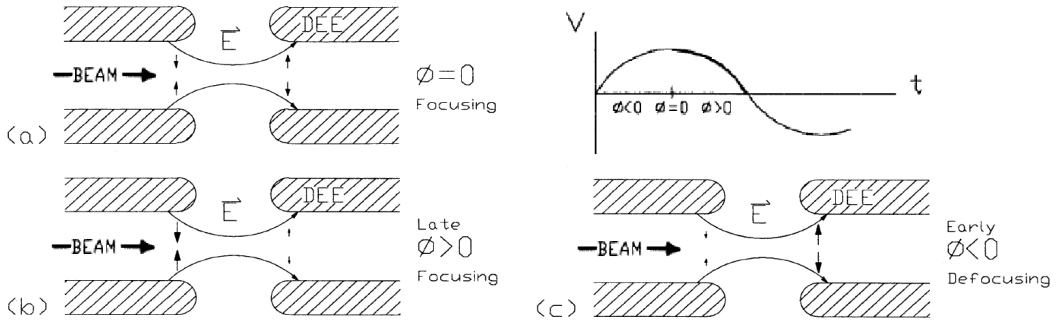

Figure 2.7: An illustration explaining the mechanism of electric focusing occurring in the central region.

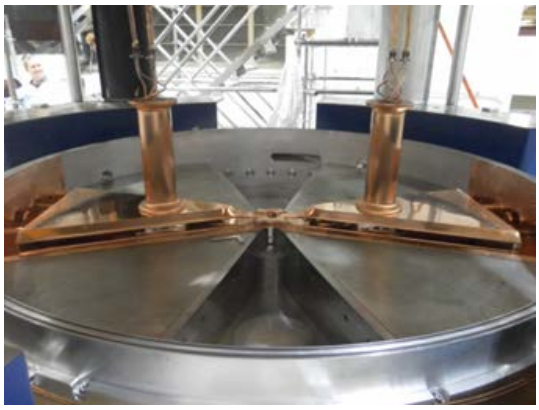

Figure 2.8: Picture of the two radiofrequency cavities of SPES cyclotron.

across the gaps formed by the electrodes carrying the electric potential and the grounded electrodes.

In the SPES cyclotron there are two dees with triangular shape settled in the space of two opposite valleys and forming four accelerating gaps with the surrounding ground electrode (see Figure 2.8). The four stems (only the upper two are visible in the picture) are part of the resonant structures and the lateral cut is necessary for the passage of accelerated particles. The radiofrequency high power signals come from two transmission lines connected by means of couplers to the lateral sides most distant from the cyclotron center. The dees are designed as two independent radiofrequency $\lambda/2$ resonant cavities operating at the 4^{th} harmonic of cyclotron frequency.

The electromagnetic signals are provided by two radiofrequency power systems connected with the resonant cavities through couplers that inject the electromagnetic power into the cavities. The power required at full beam intensity is about $55\,kW$ for each cavity.

From the point of view of the simulation of the central region only the tips of the cavities are included in the virtual model. The potential applied to them was considered uniform and varying with time as:

$$V_1 = V_{1_0}\cos(\omega_{RF}t) \qquad V_2 = V_{2_0}\cos(\omega_{RF}t + \phi_{21}) \tag{2.11}$$

where three parameters can be adjusted during cyclotron operation, once the radiofrequency is fixed to the value of $f_{RF} = \frac{\omega_{RF}}{2\pi} = 56.16\,MHz$: the amplitude of the two signals, V_{1_0} and V_{2_0}, that can be varied up to $61\,kV$,

the phase difference ϕ_{21} of the second signal with respect to the first. The energy gain per turn can be expressed as:

$$\Delta E = 2N_{dee}\, qV_0\, sin\left(\frac{h\,\theta_{dee}}{2}\right) \tag{2.12}$$

where N_{dee} is the number of dees, h the harmonic number and θ_{dee} the dees azimuthal extent. For SPES cyclotron $\theta_{dee} = 45\,deg$ and hence the maximum energy gain is achieved for $h = 4$ with cavities operating in phase ($\phi_{21} = 0\,deg$), or push-push configuration.

2.4 THE SIMULATION WORKBENCH

The cyclotron central region is added as a block in the Simion workbench of the injection line in order to run the entire simulation of particle dynamics from the source to the third turn into the cyclotron where it is stopped on the pop-up probe.

The central region is formed by two potential arrays, one of magnetic type for storing the magnetic field map of the central region and the other one of electric type for importing the geometry of electrodes (inflector, ground and dees).

The computation of the magnetic field was performed using Opera software suite where a virtual model of the cyclotron was available. The magnetic field map was exported as a csv file and then converted into the format required by Simion. The field map covers a volume of $40\,mm \times 300\,mm \times 300\,mm$ with $1\,mm$ resolution. In Figure 2.9 the color map representing the magnetic field intensity on the median plane. The hills and valleys are the red and blue regions where the magnetic field is higher and lower. On the median plane only the axial component of the magnetic field is present.

In the case of electric fields a different approach was used. The geometry of all the electrodes (two for the inflector, two for the dees, one for the ground) was imported from the stl file of the cyclotron 3-dimensional model with resolution of $0.5\,mm$ and the computation of the electric field was performed by solving Laplace equation. The presence of electrode geometry in the workbench, besides electric field map alone, is necessary to study particle loss during the injection process. The geometry of the central region electrodes is indeed quite complex as can be seen in Figure 2.10. After the

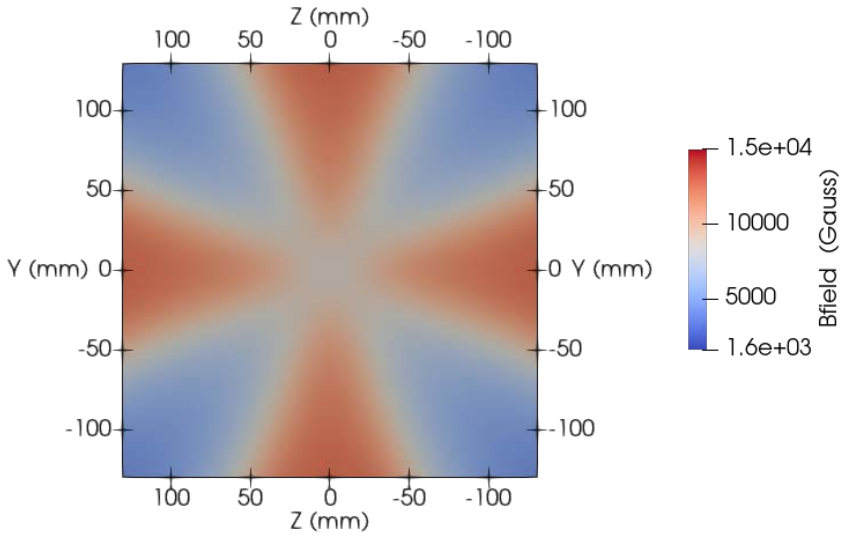

Figure 2.9: Magnetic field intensity map on the median plane.

inflector, particles on the first turn have to pass through two channels, one for each dee.

To keep agreement with the reference frame already used in the injection line workbench, the axial direction is represented by the x axis, while the median plane of the cyclotron lies in the yz plane located at $x = 2243.1\,mm$ from the ion source.

Particle information was recorded on a sequence of stages defined in the Simion Lua script as planes passing through the cyclotron center and perpendicular to the median plane, the angle θ of each stage plane being specified with respect to the y axis. A compromise to smoothly follow particles, without exceeding in the resulting file weight, was the choice of a step angle of $\Delta\theta = 360/64\,deg$, so that the spiral trajectory of each particle was sampled exactly 64 times per turn. In addition to the azimuthal angle θ, the turn number $n = \theta/360$ is also a useful variable to follow the particles along their spiral path.

2.5 SIMULATION RESULTS

The simulation of the beam dynamics in the central region is now presented.

The beam running in the following simulations is the same beam that was used in the previous chapter for the simulation of the injection line. It contains 12000 particles at the beginning. Unless specified, the voltage

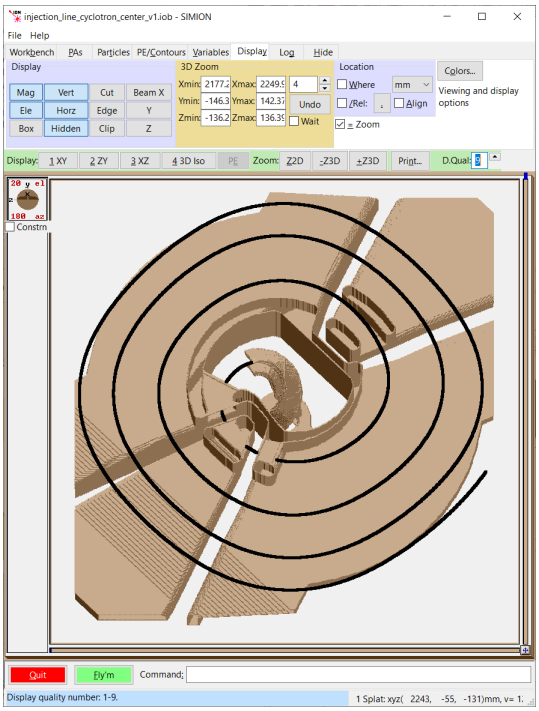

Figure 2.10: Simion rendering of the central region with a single particle track. The complexity of the geometry is put in evidence by cutting away the top part in the visualization.

amplitude is set to 61 kV for each dee and the phase difference between the two signals is set to 31.5 deg. These were indeed the optimal experimental values found during the machine operation for central region study, stopping the beam on the internal probe. During normal operation the optimal phase for extracting the beam is 0 deg as implied by the isochronous condition.

This non-null phase difference between the two cavities compensates for the lack of isochronism of particles in the first turn after beam injection due to the magnetic field bump in the central region. Indeed, according to (2.7) and considering a magnetic field bump of about 200 G over the isochronous field of 9200 G, we get approximately:

$$\Delta\phi = 360 \cdot h \cdot \frac{\Delta B}{B} \approx 31\, deg \tag{2.13}$$

The kinetic energy of the source beam was approximated to a gaussian with 1 eV of standard deviation. The time distribution of the particles was considered uniform into an interval equal to a single radiofrequency period. This assumption is motivated by the fact that the dynamics is periodic. We

are simulating and analyzing the dynamics of particles forming a single bunch.

2.5.1 *The longitudinal dynamics: energy and phase distribution. Phase acceptance.*

Particles are injected through the inflector with uniform time distribution to reproduce the real steady flow of particles in one radiofrequency period, about 18 *ns*. When they approach the first accelerating gap within the correct time window with respect to the radiofrequency signal, they gain enough energy to pass the two channels and can be accelerated turn by turn as it is shown on the left side of Figure 2.11. The kinetic energy of particles is represented as a function of turn into the central region, showing how particles gain energy when repeatedly passing through the accelerating gaps.

On the other hand, if particles, arriving at the first gap, fall outside the acceptance time interval, they do not get enough energy to pass the channels or they get negative energy gain, being decelerated. This process selects the incoming particles based on their incoming phase with respect to the radiofrequency.

The left plot of Figure 2.11 represents the kinetic energy of every simulated particle as a function of the number of turns inside the central region. Each line corresponds to a single particle and the transparency of lines is used to highlight the kinetic energy distribution of beam particles at every turn value. The color intensity due to line superposition is indeed proportional, for every turn value, to the number of particles populating a certain energy interval. The first point of the plot corresponds to the exit of inflector. At the first gap half of all the injected particles is accelerated by the electric field, the remaining part being decelerated. After passing the second gap, only a portion of the accelerated particles survives and can reach the third gap. Once completed the first turn, no further significant losses occurs in the central region. This selection process will be highlighted in the next paragraph.

The situation repeats equal to itself at every radiofreuqency period. The continuous flux of particles entering the cyclotron is transformed into a train of bunches containing only a little fraction (around 10%) of the input

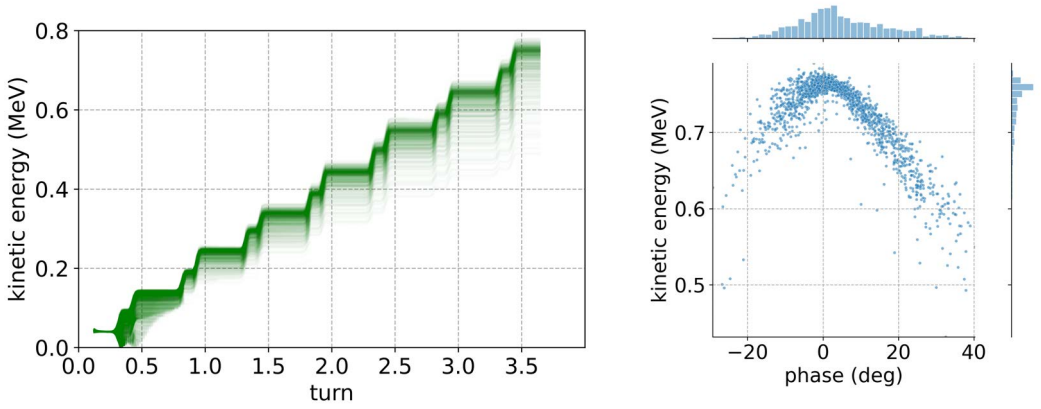

Figure 2.11: On the left, plot of kinetic energy of the particles as a function of the turn into the central region. On the right side, the phase-energy scatter plot of particles at the arrival plane at turn 3.75.

particles, the others being rejected at the entrance of the machine. The number of bunches settling in every turn is equal to the harmonic number. The structure of a beam extracted from a cyclotron is finally not a continuous flux of particles as the one generated by our ion source, but, instead, a sequence of pulses with duration of few *ns* each and repeating every radiofrequency period.

Figure 2.12 illustrates the time structure of a beam circulating in the cyclotron by means of the simulation of an incoming continuous beam within a time interval of 3 radiofrequency periods. The left plot represents the time histogram of particles collected at the last stage (turn 3.75). The right plot, instead, represents a snapshot of the particle positions on the median plane at a fixed time instant, showing multiple bunch formation in the first turn.

On the right side of Figure 2.11, the phase-energy distribution of particles collected on the arrival plane shows how the phase interval shrinks from an entire period of about 18 *ns* before injection to a little fraction of it, around 3 *ns*, corresponding to 60 *deg* of radiofrequecy[3]. The energy distribution is significantly asymmetric exhibiting a long tail towards the lower energies. The reason of this particular phase-energy distribution is that both particles arriving before and after the electric field peak within the acceptance interval

3 The conversion from time to phase variable is done by putting $\phi[deg] = 360 \cdot f_{RF} \cdot t$

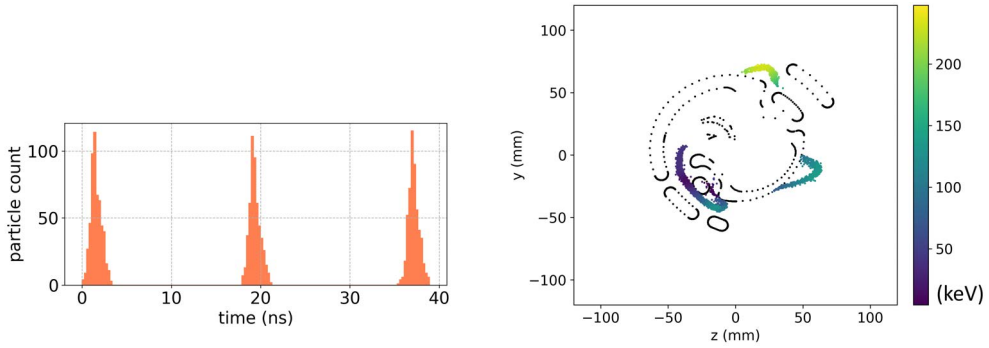

Figure 2.12: Illustration of the time structure of a beam circulating in the cyclotron (on the left) and multiple bunch formation in the first turn (on the right).

are transmitted ahead. A strict upper limit to the energy distribution is due to the fact that no particles can gain more energy than the amplitude of the accelerating electric potential. Generally, the energy distribution versus the phase can be derived from (2.7) and (2.12):

$$\frac{\Delta E}{\Delta \phi} = \frac{1}{2\pi}\left(\frac{\omega_{rev}}{\omega_{RF} - h\,\omega_{rev}}\right) qV_0 cos(\phi) \tag{2.14}$$

To determine the acceptance interval, the statistical distribution of the input phase of the particles survived at the end is plotted in the histogram of Figure 2.13. Two times the standard deviation of that distribution is assumed to define the acceptance phase interval, that is about $60\,deg$ of radiofrequency.

2.5.2 *Transmission and particle losses*

Due to a limited acceptance interval, the majority of particles are lost in the first turn when passing through the channels. In Figure 2.14 the lost particles are represented as transparent dots with color corresponding to their energy.

The transmission T_{stage} can be computed at every recording plane, or stage, as the ratio between the number of recorded particles N_{stage} at that stage and the initial number of particles in the simulation (from the ion source) N_{source}. This is indeed what is represented in the bar plot of Figure 2.14.

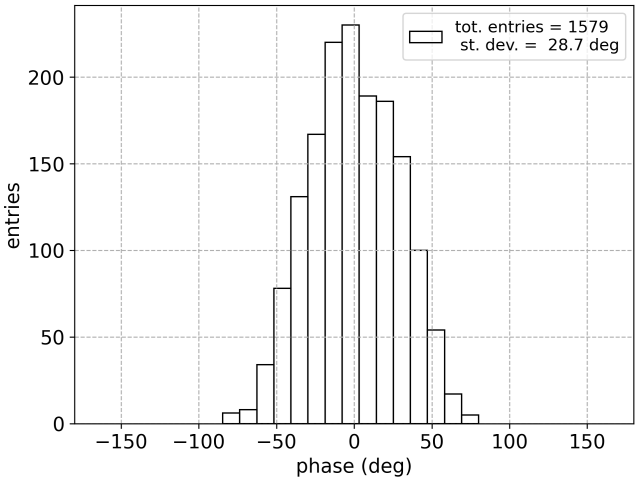

Figure 2.13: Histogram of the initial phase of the particles at the arrival plane. For a dee voltage of 61 kV and phase difference of 31.5 deg the acceptance interval is about 60 deg.

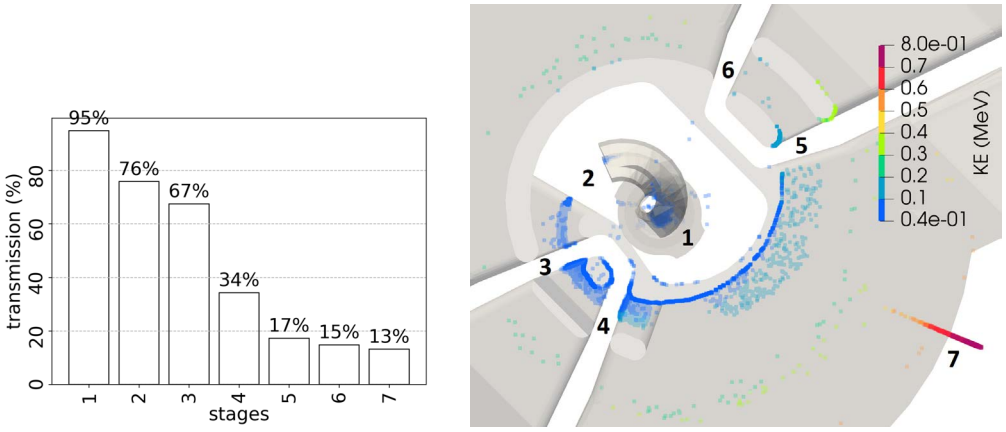

Figure 2.14: On the left, transmission computed at several recording stages inside the central region. On the right, ions lost inside the central region with their energy represented by the color scale.

For the sake of a clear representation, only some key recording planes are considered (see Figure 2.14), corresponding to: the collimator at the end of the injection line before the inflector entrance (1), the inflector exit at $\theta_2 = 45\,deg$, the first passage through the four accelerating gaps (3 to 6) at angles $\theta_3 = 112.5\,deg$, $\theta_4 = 157.5\,deg$, $\theta_5 = 202.5\,deg$, $\theta_6 = 247.5\,deg$, and the arrival plane (7) at turn $n = 3.75$.

Equivalently, transmission can be defined as the ratio between the beam current observed through a certain recording plane I_{stage} and the source beam current I_{source}:

$$T_{stage} = \frac{N_{stage}}{N_{source}} = \frac{I_{stage}}{I_{source}} \tag{2.15}$$

This quantity is the most important to be calculated from the simulations in the perspective of a comparison with the experimental data, as we are going to see in the following two paragraphs. Indeed, both the beam current extracted from the ion source and the beam current at the pop-up probe were measured during cyclotron operation and transmission were studied as a function of the operational parameters of the machine: dee voltage and phase difference.

With the optimal parameters found during operation of the cyclotron when stopping the beam on the probe inside the machine ($31.5\,deg$ dee phase difference and $61\,kV$ dee voltage amplitude), the value of transmission observed experimentally is 14%. This value is reasonably comparable with the transmission $T_7 = 13\%$ computed from the simulation at the last recording stage (7). To compute the experimental transmission we measured a source current of $I_{source} = 2.5\,mA$, that was attenuated of factor 40 by a pepper pot device inserted in the spare vacuum chamber of the injection line[4], while reading a corresponding beam current on the pop-up probe of $I_{probe} = 8.6\,\mu A$, as also reported in the experimental plot of Figure 2.16:

$$T_{probe} = \frac{I_{probe}}{I_{source}/40} \tag{2.16}$$

4 In the position where optional devices can be inserted (see Figure 1.1).

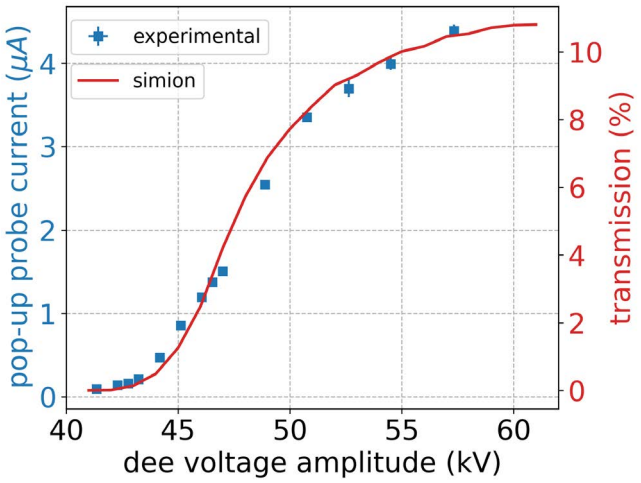

Figure 2.15: Transmission as function of dee voltage amplitude for a fixed phase difference between dee signals of 6 *deg*. The experimental voltages are multiplied by scaling factor of 0.94.

2.5.3 *The dee voltage amplitude*

The phase acceptance of the cyclotron is not a fixed parameter, but depends, within some limits, on the amplitude of the accelerating voltage and on the phase difference between the two oscillating voltages.

There is a certain threshold level of the dee voltage amplitude below which no particles can be transmitted because they would gain too low kinetic energy and the curvature radius of their trajectories would be less than the minimum allowable by the electrode geometry. Above that value the transmission increases with the voltage reaching a maximum. In the plot of Figure 2.15, the data taken during cyclotron operation are compared with the results of simulations. A scale factor on the dee voltage have to be found empirically to make the simulations to match the real data. This is because the dee voltage displayed in the control system of the cyclotron is only indicative but not exactly the real value of the voltage in the central region. The value found for the scaling factor is around 0.94 so that the real value of voltage in the central region should be 0.94 times the value displayed in the cyclotron control system.

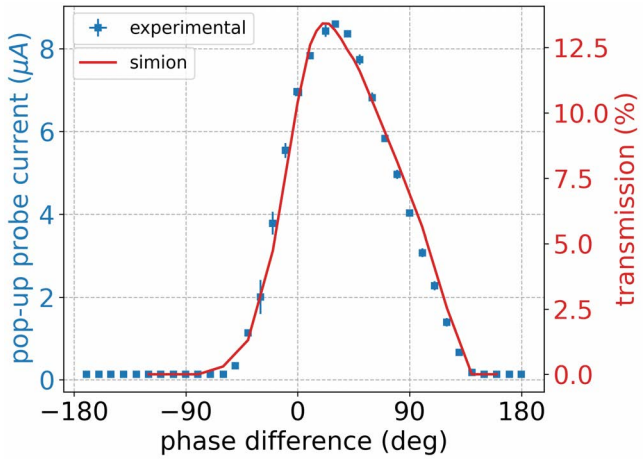

Figure 2.16: Transmission as function of phase difference between dee signals with fixed dee voltage amplitude of 61 kV. The maximum transmission occurs at around 31.5 deg.

2.5.4 *The phase difference*

The acceptance interval varies with the phase difference between the accelerating voltage of the two dees.

It is experimentally verified that in the central region the largest acceptance occurs for a phase difference of 31.5 deg measured directly with an oscilloscope of 200 MHz bandwidth. At this angle the maximum transmission is observed also in the simulations that are put in comparison with the experimental data collected during cyclotron operation, showing good agreement (see Figure 2.16).

A non-null optimal value of phase difference between the dees is observed only when the beam is stopped in the central region and measured with the pop-up probe. Instead, during normal cyclotron operation the extracted beam current is maximum with null phase difference between cavities as should be to fulfill the isochronous condition. This effect is due to the magnetic field bump in the central region where the magnetic field is higher than the isochronous value.

The phase slip of particles with respect to the radiofrequency can be computed for each piece of trajectory, starting from the center of the first gap, by the general formula:

$$\Delta\phi = \Delta t \cdot \omega_{RF} - \Delta\theta \cdot h \tag{2.17}$$

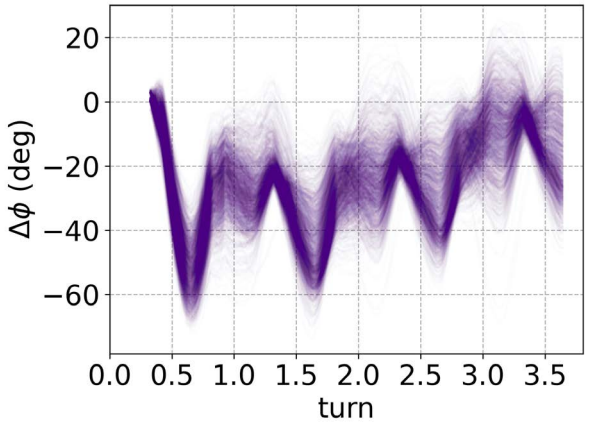

Figure 2.17: Phase history of the particles assuming the starting point in the center of the first accelerating gap.

where Δt is the observed time taken by the particles to travel a fixed angle of $\Delta\theta$. The resulting phase history of particles is shown in Figure 2.17. The mean value remains close to the expected $30\,deg$ and reduces progressively as the mean magnetic field goes towards the isochronous value.

Part II

DEVELOPMENT OF THE BUNCHER DEVICE

In the second part the design of a buncher device is conceived for future implementation. Beam dynamics simulations are performed to estimate the improvement in the injection efficiency and to define the better configuration of the component. Finally, the electronic chain for buncher operation is studied.

3

THE BUNCHER DEVICE

We now move to the description and simulation of the buncher device that have to be designed to fulfill the specific requirements of our injection system.

3.1 ADVANTAGES OF INTRODUCING THE BUNCHER DEVICE

As already pointed out in the introduction, the buncher device can significantly improve beam injection efficiency (IE), which is defined in our case as the ratio of beam current I_{probe} measured at the pop-up probe and the beam current I_{source} provided by the ion source. Alternatively, the total number of particles collected at the pop-up probe N_{probe} and those coming from the ion source N_{source} during a certain fixed time interval can be considered instead of beam current:

$$IE = \frac{I_{probe}}{I_{source}} = \frac{N_{probe}}{N_{source}} \tag{3.1}$$

The latter definition is easier to use in the simulations, while the former is more useful when dealing with experimental measurements. As defined above, injection efficiency IE is nothing else than beam transmission 2.15 evaluated between the ion source exit and the pop-up probe. Sometimes could be more intuitive to express IE in percentage instead of a ratio.

Several benefits can be addressed from improving IE. First of all, a certain value of beam current could be extracted from the cyclotron with less current provided by the ion source, preserving the ion source from material degradation, in particular the tungsten filament, and then reducing maintenance operations. Alternatively, if high intensity beams are needed for applications, more current can be extracted from the cyclotron with the same current provided by the ion source.

Another use of the buncher to be evaluated experimentally is to regulate the beam intensity by slightly change the operational parameter of the buncher (phase difference with respect to the cyclotron radiofrequency

and voltage amplitude across the buncher electrodes). Up to now, the only parameters which can be changed to regulate beam current being extracted from the cyclotron are: the ion source parameters (arc current and extraction electrode voltages), the cyclotron cavity voltages and phases. None of them should be changed for optimal operation of the systems, so that beam current regulation should be addressed by a specific component. The buncher could be suitable for that scope within certain limits that have to be investigated experimentally, such as the resolution with which the extracted beam current could be varied, and the total achievable range of the extracted beam current.

3.2 DESCRIPTION OF THE COMPONENT AND ITS WORKING PRINCIPLE

The buncher working principle is now explained starting from the simplest ideal case and then moving towards a practical design.

3.2.1 *Single gap buncher*

An ideal buncher device would compress a continuous beam into packets (bunches) of particles arriving all at the same time to a focusing point located at a certain distance from the device.

To have a physical picture of the bunching process we can think of a continuous beam entering the buncher device as an ensemble of particles with initial times uniformly distributed within an interval of one cyclotron radiofrequency period and all moving along the same direction with the same velocity $v << c$ [1]. If no action was done on the beam, the particles would reach with the same time distribution any point along the direction of motion.

We want the buncher device to modulate the longitudinal kinetic energy of particles passing through it in order to make them arriving all at the same time instant t after traveling a certain distance L. If this distance is much bigger than the buncher device length, we can think of it as infinitely thin.

1 We are assuming that any relativistic effect is negligible and kinetic energy can be expressed by the classical formula $E = mv^2/2$

A simple kinematic exercise can be done to determine the kinetic energy gain ΔE required by the particles as a function of their advance (or delay) from an ideal reference particle which travels the distance L in time t with velocity v:

$$L = vt$$

This reference particle exits the buncher device with unmodified velocity. What we require is that any other particle, exiting the buncher device with a certain advance Δt (or delay $-\Delta t$) and moving with a slightly different velocity v', would reach the same point in L at the same time instant t:

$$L = v'(t + \Delta t)$$

Solving the system of two equations leads to:

$$v' = v\frac{t}{t + \Delta t} = v\frac{L}{L + v\Delta t}$$

and, after some algebraic steps, to:

$$\Delta E = E' - E = E\left(\left(\frac{L}{L + v\Delta t}\right)^2 - 1\right) \approx -2\frac{v}{L}E\,\Delta t \tag{3.2}$$

In the last step the energy variation ΔE is considered as a function of the time advance Δt and is approximated with a linear function in a small interval around $\Delta t = 0$ using the well known first-order Taylor expansion $\Delta E(\Delta t) = \Delta E(0) + \Delta E'(0)\,\Delta t$, where $\Delta E'(0)$ is the first derivative of ΔE with respect to Δt computed in $\Delta t = 0$.

In our case we have H^- ions with mass $m = 938\,eV/c^2$, kinetic energy $E = 40\,keV$ and speed $v = 2.76 \cdot 10^6\,m/s$, traveling the distance $L = 1.35\,m$ and being distributed in an interval of one radiofrequency period $\Delta t \in [-9, 9]\,ns$, so we get $\Delta E \in [-1500, 1500]eV$. In figure 3.1 is reported the plot of kinetic energy gain as a function of time advance. The reference particle has zero time delay and gets no energy gain, particles arriving in advance ($\Delta t > 0$) are slowed down, particles arriving in delay ($\Delta t < 0$) are accelerated.

Finally, an ideal buncher device should make the particles gaining a kinetic energy ΔE almost proportional to their time advance Δt with respect to an ideal particle which passes undisturbed through the device.

The performance of a buncher device is quantified by the bunching efficiency BE. It can be defined as the number of particles N_x arriving within

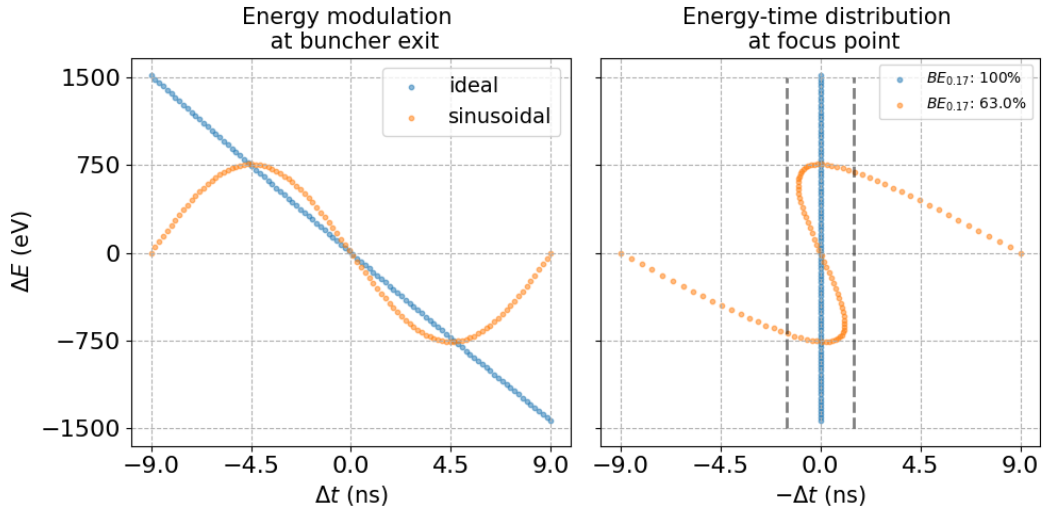

Figure 3.1: On the left, energy modulation ΔE, as function of time advance Δt with respect to the reference instant, of particles exiting an ideal saw tooth buncher (blue dots) or a sinusoidal buncher (orange). On the right, the distribution of particles at the focus point. The dashed vertical lines indicate the $3\,ns$ interval of cyclotron acceptance.

a certain time window (or period fraction $x \in [0,1]$) around the reference time instant over the total number of particles N_1 that entered the device in one period:

$$BE_x = \frac{N_x}{N_1} \tag{3.3}$$

In our case the reference period fraction is $x = 60/360 \approx 0.17$, given the $60\,deg$ phase acceptance interval of the cyclotron.

From the practical point of view, a buncher device like that discussed above should be designed to have a single accelerating gap and a saw-tooth electric signal $V(t)$ applied across it. Several devices of this kind can be found in the literature [24] [25].

In practice, only an approximation can be implemented of such a saw-tooth function with amplitude V_0, adding a certain number of harmonics, in agreement with the Fourier series expansion:

$$V(t) = \frac{V_0}{2} \sum_{k=1}^{n} (-1)^k \frac{\sin(2\pi f_{RF} t)}{k} \tag{3.4}$$

This approach could lead to the highest possible efficiency, ideally 100%, but non trivial complications from the point of view of the radiofrequency system driving the device.

A simpler implementation would make use of the first harmonic alone out of the saw-tooth expansion. In this case, the electric potential is a sinusoidal function with half the saw-tooth amplitude:

$$V(t) = -\frac{V_0}{2}\sin(2\pi f_{RF} t) \tag{3.5}$$

where $V_0 = 1500\,V$ in our case. The energy modulation of particles, just after passing through the device, will approximate the ideal linear behavior only within half the period. This implies that only those particles will be collected in the bunch, roughly half of the total number of them. If we compute the bunching efficiency in our case of $60\,deg$ phase acceptance interval, that corresponds to 17% of one period, we found an ideal 63% bunching efficiency (look at Figure 3.1).

3.2.2 *Double gap buncher*

Another approach to realize a sinusoidal buncher comes from the consideration that energy modulation could be achieved in more than a single step. The idea is to use two accelerating gaps instead of only one, so that the resulting device resembles a very short Wideroe linac driven by a sinusoidal signal. Devices of this type are also well documented in the literature [26] [27] [28] [29].

According to an ideal situation, in the case of two gaps, the energy modulation should follow a triangular profile, instead of a saw-tooth, and with half the amplitude, because the particles traveling from the first gap to the second gap should find the same potential but with reversed sign to find the electric field pointing in the same direction, energy gain being achieved in two steps. The only possible periodic signal that could drive this device is in fact a triangular wave and such a signal is very well approximated by a simple sinusoid. The plot of Figure 3.1 shows that only the particles within the central half period will gain the proper energy to reach the focus point together, while the particles outside that interval will not get enough energy to arrive at the focus point within the prefixed time window.

The obvious advantage of this structure is that the required amplitude of the electric potential can be halved, leading to less demanding requirements for the electronics system implementation. The only drawback is that the maximum theoretically achievable efficiency is limited to a bit more than half of the saw-tooth case, because only particles contained in the central half period are effectively bunched, and cannot be significantly extended by adding further harmonics.

The basic constraint to be fulfilled on the design of a two gap buncher is the distance between the accelerating gaps. It should be fixed to an odd multiple of $\beta\lambda/2 = vT/2$, the distance traveled by the reference particle in half of the radiofrequency period $T = 1/f_{RF}$, where $\beta = v/c$ is the speed of particle divided by the speed of light in vacuum and $\lambda = cT$ the wavelength of the radiofrequency signal in vacuum.

3.2.3 *Transit Time Factor (TTF)*

Up to now we have studied in the simplest case the effect of kinetic energy modulation on particles moving along a linear path.

Going towards the practical implementation of a buncher device that would impress the desired energy modulation to the ions passing through it, another relevant concept to study is the so called Transit Time Factor (TTF), which comes from linac theory. It produces an unavoidable though unwanted effect in the operation of any radiofrequency accelerating structure (not only linacs) and should be maximized in the design of our buncher, as soon explained.

The transit time factor is defined as the ratio between the total kinetic energy gained by a particle passing through the device over the total kinetic energy gain it would have if the electric field would act statically [30]:

$$TTF = \frac{\int E(z)\cos\left(\omega z/v + \phi_{in}\right) dz}{\int E(z) dz} \tag{3.6}$$

To understand formula (3.6), let us consider a sinusoidal buncher device with a single gap where the electric field oscillates in time with angular frequency ω. An ion moving with velocity v along the z axis and passing through the buncher device with a certain time advance ϕ_{in}/ω will experi-

ence a total potential variation that we can divide by the total static potential variation. Moreover, the electric field z component have a certain distribution along the z axis and its amplitude $E(z)$ can be indeed represented as a function of z, usually a bell shaped function with certain width.

The transit time factor is due to the fact that the electric field is not static but changes with time so that the particle will experience a net force that is always less than the static force, the TTF being always less than unity. It depends on the electric field spread in the particle direction of motion.

To keep the TTF as high as possible, the electric field should spread in space as little as possible. This is clear when considering that, if the electric field followed a δ-Dirac distribution (null width), TTF would be equal to 1, the maximum allowable value.

To better understand the concept, let us consider a single accelerating gap and a particle traveling through it along the z axis. Across the gap located at $z = 0$ we can reasonably represent the static electric field z component as a normal distribution function with a certain spread σ:

$$E_\sigma(z) = \frac{1}{\sqrt{2\pi}\sigma} e^{\frac{-x^2}{2\sigma^2}} \tag{3.7}$$

the integral of this function along the z axis is always equal to 1.

Provided that the electric field oscillates harmonically in time with frequency ω, a particle with initial phase $\phi_{in} = 0$ and moving with velocity v (supposed to be constant) along the z axis would experience an electric field given by:

$$E_\sigma(z,t) = E_\sigma(z)\cos(\omega t) = E_\sigma(z)\cos(\omega z/v) \tag{3.8}$$

time t being equal to z/v. It is also to be noted that a characteristic distance can be defined as $\beta\lambda = vT$ the distance traveled by the particle during a period of oscillation.

The integral of $E_\sigma(z,t)$ along z is the energy gained by the particle over its electric charge and also coincides with the transit time factor because $E_\sigma(z)$ is normalized to 1.

In the picture of Figure 3.2 the electric field seen by the particle and the corresponding integral (or TTF) is computed for several values of σ using as length unit the distance $\beta\lambda$. With this choice the plot is general and can be applied to any particular design with different frequency, particle velocity and field spread.

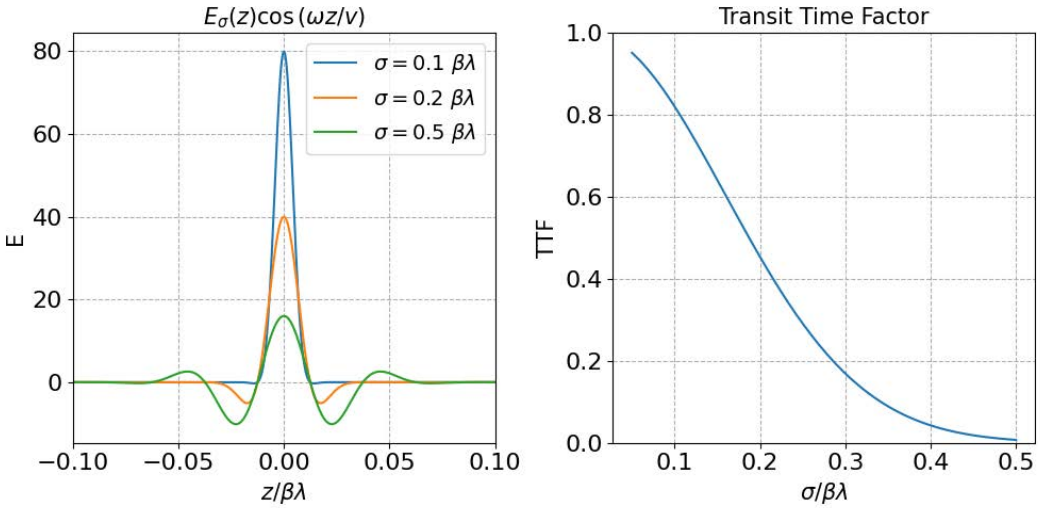

Figure 3.2: Transit time factor computed as the integral of the electric field seen by a particle moving on the central axis of a single accelerating gap for several values of σ.

For instance, if the spatial spread of the electric field across the gap and the velocity of particles are fixed quantities, the transit time factor increases with frequency because the characteristic distance $\beta\lambda$ proportionally reduces. This effect could be relevant in a single gap buncher device driven with more harmonics.

3.3 DEVELOPMENT OF A BUNCHER COMPONENT

The only constraint for the realization of a buncher device for the SPES cyclotron is due to the characteristics of the vacuum chamber where it will be installed, so that the total length of the device cannot exceed 120 mm.

Although a single gap buncher could be a good choice because of its compactness, using more than a single harmonic would require a complex radiofrequency system to drive it. Instead, a double gap device, even if its bunching efficiency is limited, as discussed before, needs a simpler and cheaper electronic system. It requires less power and easier matching circuit, as will be discussed in the next chapter. For that reasons we begin to develop a double gap device.

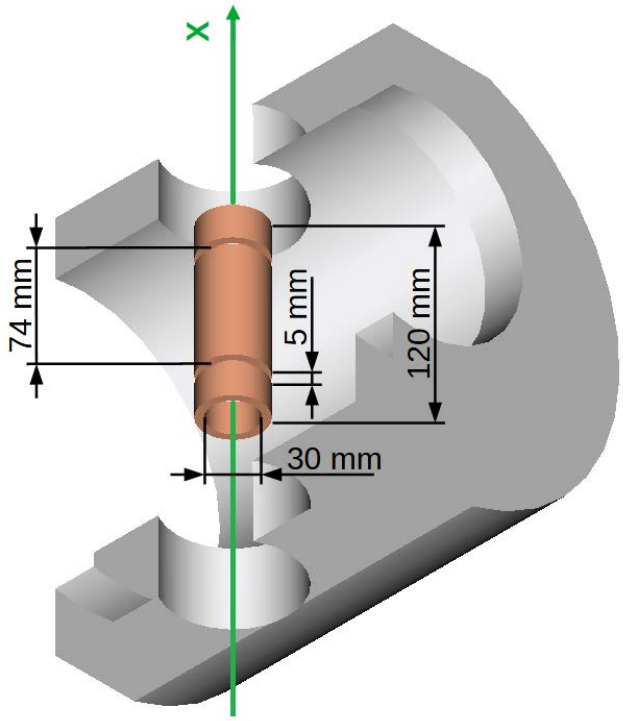

Figure 3.3: Simplified mechanical model of the buncher used for the electric field computation. The device is located in the spare vacuum chamber of the injection line and the beam direction x is represented by the green line. The value of the geometric parameters are reported directly on the picture.

The device is designed as follows. It is composed of three short metallic tubes placed along the beam line and spaced from each other to form two gaps, as shown in Figure 3.3. The distance between the center of the two gaps (not the central electrode length) is fixed to $3\beta\lambda/2 = 74\,mm$, the characteristic length being $\beta\lambda = v/f_{RF} = 49\,mm$. The central electrode brings the radiofrequency signal and the side electrodes are grounded. Other possible implementations of the device are discussed in the last paragraph and compared with each other.

The internal diameter and the gap between the electrodes should be now chosen as little as possible in order to maximize the TTF.

From the beam envelope simulation of the injection line in Figure 1.7 it follows that the buncher internal diameter can be safely not smaller than $30\,mm$.

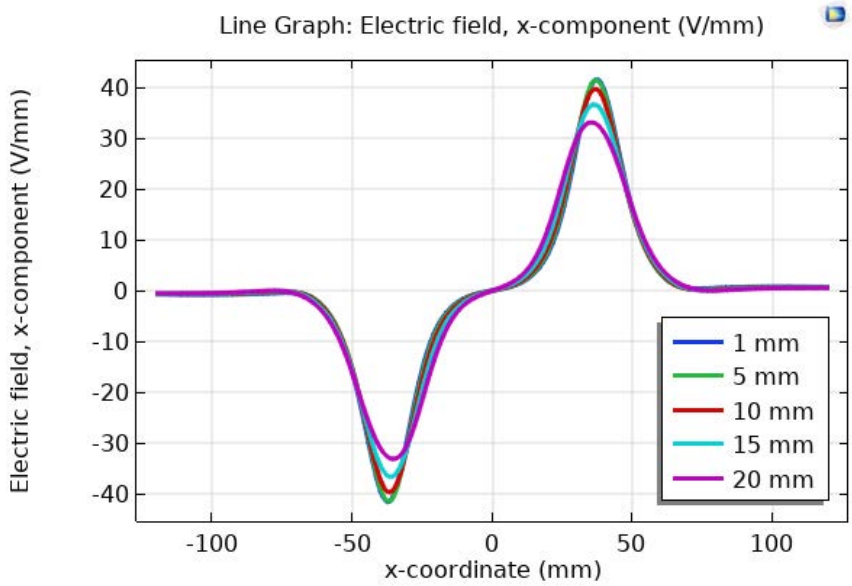

Figure 3.4: Static electric field along the central axis of buncher with gap taken as parameter. The central electrode is set at 1000 V and the side electrodes at ground.

As can be seen from the parametric electrostatic simulation in Comsol (Figure 3.4), a gap of 5 mm is sufficient to keep the electric field width as little as possible on the central axis. Reducing the gap below that value does not lead to further reduction of electric field spread, this limit being due to the diameter of the electrodes. With this electric field spread of about $\beta\lambda/6$ a TTF of 0.5 can be guessed looking at the plot in Figure 3.2.

Choosing a gap of 5 mm and considering that the voltage of the central electrode would not exceed 1000 V, the maximum electric field across the electrodes would not be higher than $\approx$ 0.2 kV/mm, which is far below the expected vacuum dielectric strength (in the order of $\approx$ 10 kV/mm). Therefore, no discharge currents between the electrodes are expected at our operating conditions.

In practice, for improving the TTF a couple of very thin metallic grid could be used. Ions can pass through them and electric field is strictly confined in the gap. Because of the high beam current intensity transported in our injection line, we want to avoid the use of grids that could be subjected to material degradation and could also increase beam emittance by ion scattering.

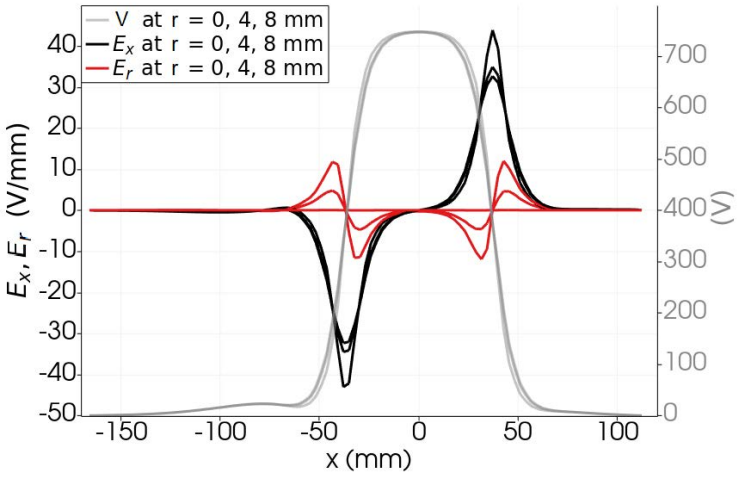

Figure 3.5: The buncher longitudinal E_x and the radial E_r electric field components and the electric potential V computed along lines displaced from the main axis by r. The potential of the central electrode is set at 1000 V.

The spatial distribution of the longitudinal electric field component E_x seen by a particle moving through the device becomes narrower, and its maximum value increases, when the line trajectory is displaced from the central axis (look at the black curves in Figure 3.5), the TTF increases consequently. This means that the particle energy modulation is more effective when they travel off the central axis.

Moreover, a radial component of the electric field E_r, that is null on the main axis, appears when considering a direction displaced from the main axis (look at the red curves in Figure 3.5). This implies that particles off the central axis can receive a small radial force, as they pass through the device, increasing with their radial displacement r and depending on their phase with respect to the electric field oscillation. As pointed out in the last paragraph, this effect seems negligible in our case, as the distribution of particles in the transverse trace spaces at end of injection line is not significantly modified by the buncher device compared with the case without buncher.

3.4 RESULTS OF PARTICLE DYNAMICS SIMULATIONS

The beam dynamics simulations are now presented with the double gap buncher described in the preceding paragraph.

To perform the simulations the same workbench described in the preceding chapters is adopted. The buncher device geometry was designed in a simplified form using FreeCAD software considering the three electrodes suspended in the vacuum chamber as shown in Figure 3.3.

To speed up the simulation, the model was imported in a separate Simion workbench only for the computation of electric field map that was exported in a reduced rectangular region of 300 mm lenght and 15 mm thickness in the transverse directions with 0.5 mm of resolution.

3.4.1 *Optimal operational parameters*

The first set of simulations are devoted to find the optimal parameters for buncher operation. The buncher voltage can be represented with an oscillating function:

$$V_B(t) = V_{B_0} \cos(\omega_{RF} t + \phi_B) \tag{3.9}$$

The two independent parameters, whose value has to be determined, are the voltage amplitude V_{B_0} and the phase difference ϕ_B with respect to the signal of the first cyclotron cavity.

This can be achieved by sweeping each parameter in the simulations and compute transmission at turn 2.625 in the cyclotron. Firstly, the voltage was swept in steps of 50 V and the optimal value of 750 V was determined, while keeping the phase fixed at 75 deg (guessed manually). Then, the optimal phase value of 80 deg was determined by sweeping the phase in steps of 20 deg over the full range and 5 deg around the maximum, while keeping the voltage constant at 750 V. The resulting plots of Figure 3.6 indicate the optimal values and also give an estimate of how much the transmission is sensitive to those values. This will be important to be considered when designing the electronics for buncher operation that will be discussed in the following chapter.

3.4.2 *Evaluation of injection efficiency improvement*

By simulating the particle dynamics from the ion source to the probe into the cyclotron we can observe the transmission improvement that we expect

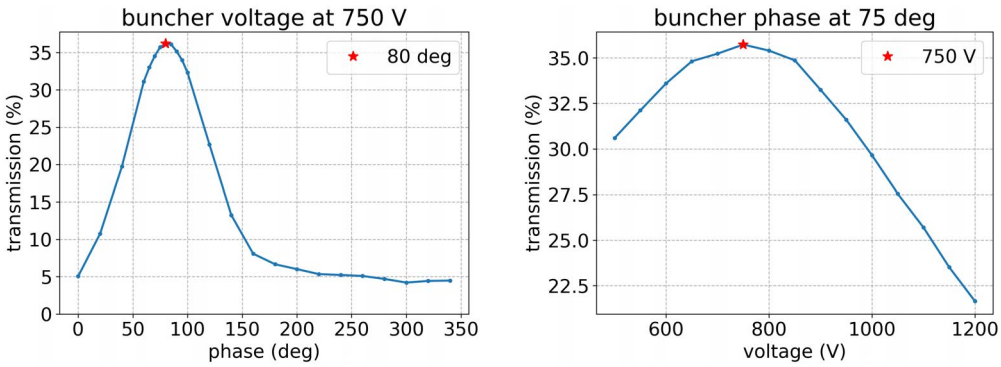

Figure 3.6: Sweep of the two operational parameters of the buncher. On the left side, transmission is studied as a function of phase difference between buncher and cyclotron signals. On the right side, as function of buncher voltage amplitude. The optimal values are those maximizing the transmission function. Transmission is computed after stopping the particles at turn 2.625.

to obtain with the buncher device operating with its optimal parameters. The plot in Figure 3.8 shows that more than twice the current intensity could be achieved in our machine. The plot of phase-energy distribution at the inflector exit (Figure 3.7) shows the expected bunching effect, the beam compression in the acceptance interval of 60 *deg* of radiofrequency with 52% of bunching efficiency over that interval. The histogram of the initial phase of particles at the arrival shows the same concept, more particles are pushed into the acceptance interval of the machine.

This result does not consider any space charge effect among the beam ions. It is reasonable when the beam current intensity is in the order of μA or less.

3.4.3 *Space charge effects and degradation of bunching efficiency*

When the beam current is in the order of magnitude of mA, the beam dynamics do not change significantly in the injection line thanks to beam neutralization. Instead, the inflector static electric field pushes away from the beam the positive ions and the beam cannot be considered neutral anymore in its following path. The space charge effects are relevant especially in the first turn in the cyclotron central region where beam energy is still low

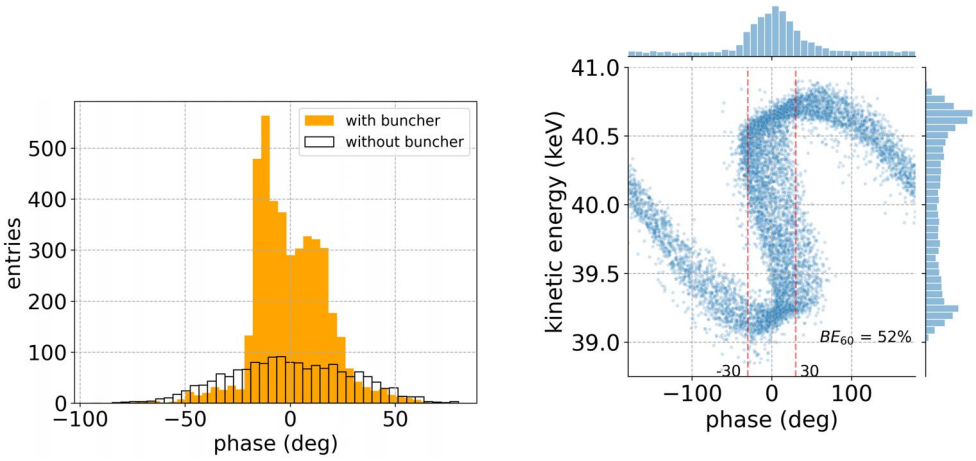

Figure 3.7: Histogram of the initial phase of particles survived at the arrival stage, comparing the case with the buncher (in orange) and without. The 60 *deg* phase acceptance interval of the cyclotron remains the same, but more particles are concentrated in it thanks to the buncher action. On the right, the energy-phase distribution of particles at the inflector exit (stage 2 referring to Figure 2.14).

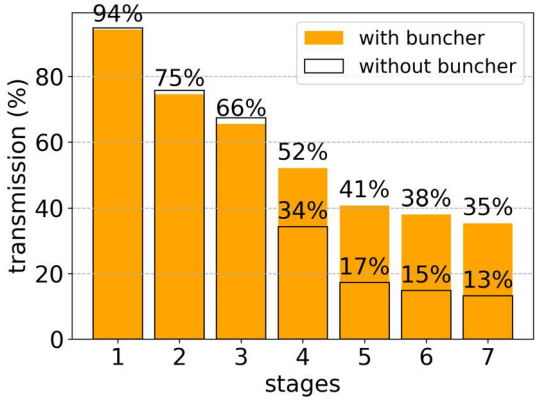

Figure 3.8: Transmission improvement in the central region of the cyclotron using the buncher device with its optimal parameters. For the list of stages refer to Figure 2.14.

and should be taken into account because they tend to counteract the beam compression operated by the buncher device.

To take into account the ion-ion repulsion, Simion provides two in-built methods for computing particle trajectories with space charge.

The "Beam" method is time independent. It models the mutual repulsion of particles within a beam by treating each particle as a current tube and applying Coulomb law between them in a transverse cross-section. This method only considers forces within the simulated plane and does not account for forces from particles in front of or behind that plane. For those reasons this method can only be used when dealing with a steady flow of particles. Just the value of beam current in Amperes has to be specified in the Simion interface.

The "Coulomb" or "Factor" methods are time dependent. They treat the beam as a cloud of point particles repelling each other in agreement with Coulomb law. Each particle represents a certain number of real particles. The "Coulomb" method requires to specify the total charge that the group of particles represents. The "Factor" method needs a multiplication factor, denoted as the Repulsion Factor RF, that multiplies the charge of each particle. The time dependent methods are obviously more general than the previous one because they deal with forces in the 3-dimensional space and not only in the transverse plane.

For our particle dynamics simulation in presence of space charge, the "Factor" method was chosen because of its simplicity. Once fixed the beam current intensity I and the number of particles N with real charge q running in the simulation, the Repulsion Factor RF is given by:

$$RF = I\frac{\Delta t}{q \cdot N} \tag{3.10}$$

where Δt is the time interval of the starting group of ions.

The space charge simulation is carried out in the part of trajectory between the inflector entrance and the first turn into the cyclotron. This is indeed the path where space charge effects are mostly relevant due to the absence of space charge neutralization and to the low beam energy.

For a realistic simulation the time interval should be bigger than a single radiofrequency period as done in the preceding simulations. This is now explained.

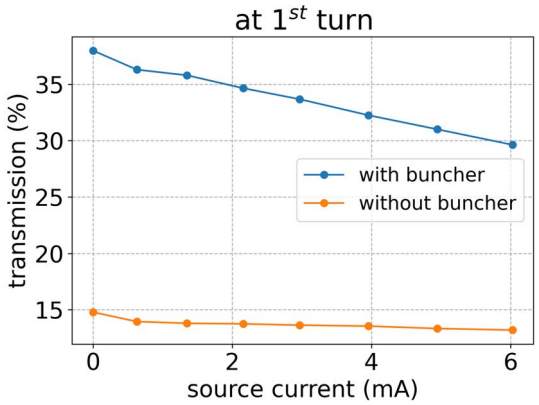

Figure 3.9: Transmission evaluated at the first turn in the central region of the cyclotron takin into account the ion-ion repulsion. With increasing the beam current intensity the transmission lowers. This effect is much more evident for a bunched beam.

When repelling each other, the particles being in the rear of the group are naturally decelerated backward by the particles staying in the core, while those in the front are accelerated forward.

In our case the beam enters the inflector as a steady flux coming from the ion source and is then broken into bunches by the electric field of the cyclotron.

To realistically model this situation an interval of three radiofrequency periods was chosen and only the central part of the group of particles was selected for the data analysis.

The effect of space charge is evident from observing the results of simulations in the plot of Figure 3.9, where the transmission is computed at the first turn as a function of beam current, showing a decrease of about 3% every mA of current increase.

In the plots of Figure 3.10 the energy-phase distribution of particles recorded at the inflector exit reveals how the space charge increases both energy and phase spread leading to reduction of the bunching efficiency.

3.5 OTHER BUNCHER DESIGNS AND CHOICE OF THE BEST CONFIGURATION

The solution explored so far is not the only possible implementation of a suitable buncher device. Remaining in the idea of a sinusoidal buncher, we

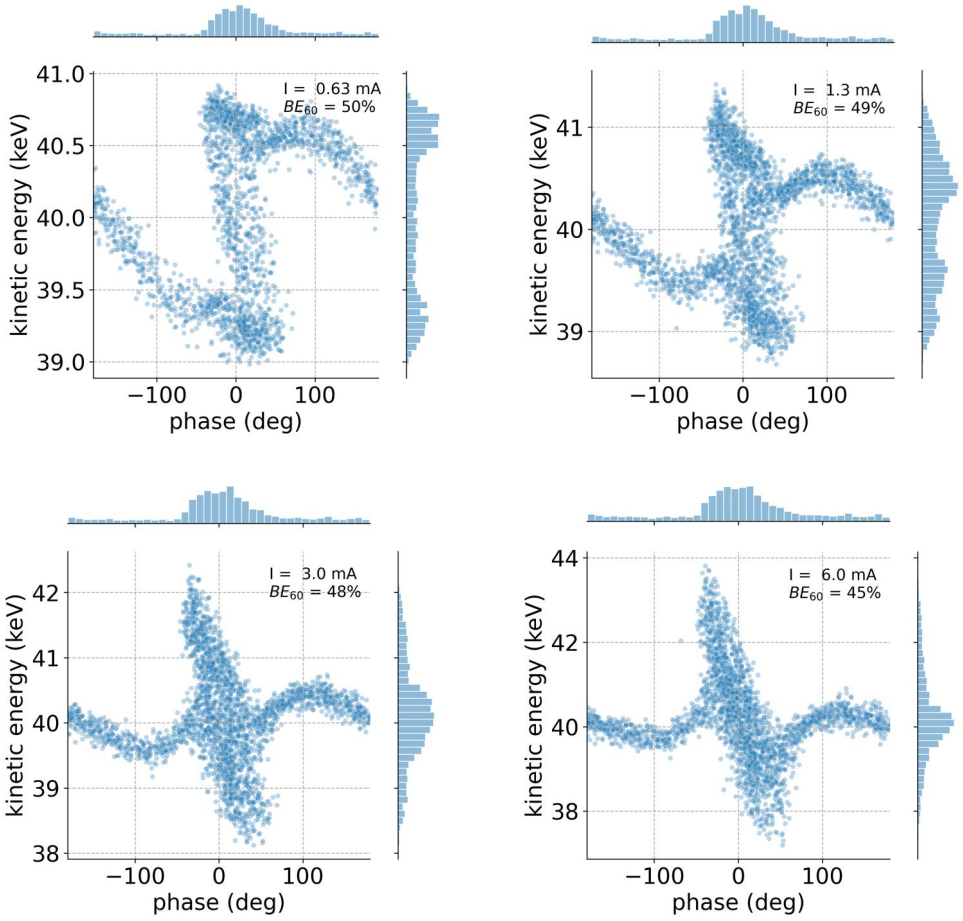

Figure 3.10: Energy-phase distribution for several current intensities recorded at the inflector exit (stage 2). When increasing the repulsion factor, the bunching efficiency reduces.

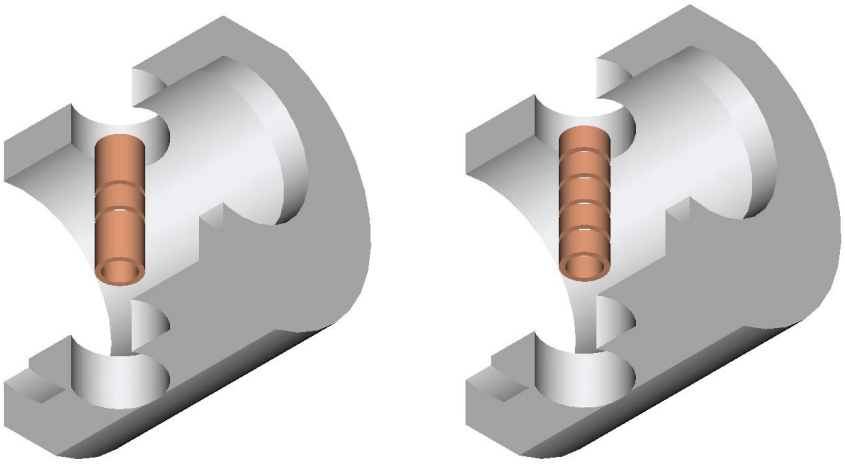

Figure 3.11: Simplified mechanical model of the other two types of bunchers. On the left, the double gap $\beta\lambda/2$ implementation. On the right, the four gap device.

can consider a double gap device with spacing between gaps of $\beta\lambda/2$, the minimal distance required for the particles to gain energy when passing through the two gaps (see left side of Figure 3.11). This solution is completely equivalent to the previous one used for the simulations, so that no advantage can be addressed to prefer one configuration against the other.

However, aiming at further reducing the required voltage, a net advantage can come from a four gap design (right side of Figure 3.11). It would be formed by five electrodes, instead of only three, with spacing between gaps of $\beta\lambda/2$, just filling the available space in the vacuum chamber. In this case the central electrode and the side electrodes are grounded and the intermediate electrodes bring the same radiofrequency signal. The optimal voltage required for proper bunching operation would be exactly $375\,V$, half of that of a double gap device, while producing the same results in terms of energy modulation, without modifying the transverse characteristics of the beam.

It is worth to directly compare the energy distribution of the same beam after passing through the three different devices, the one discussed previously and the other two. No appreciable difference can be observed in the histogram of Figure 3.12 among the three cases. Therefore, the three bunchers are equally able to modulate the beam energy as desired.

For what concerns the transverse characteristics of the beam observed at the end of the injection line ($x = 2180\,mm$) and shown in Figure 3.12, no

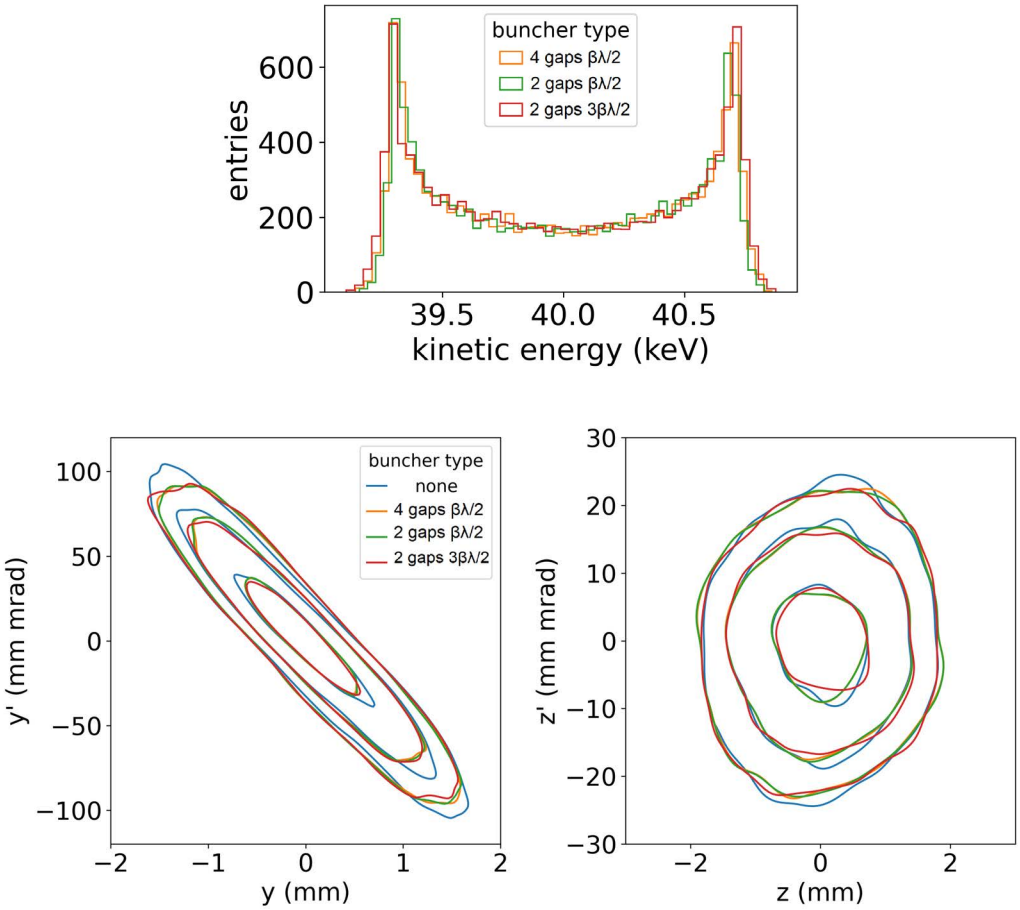

Figure 3.12: Comparison among the three buncher types. Energy distribution of particles (top) and transverse trace spaces at the end of the injection line at $x = 2180\,mm$ (bottom). The closed curves contain 20%, 40% and 80% of the particles.

significant differences can be observed among the different devices from the point of view of transverse particle dynamics. The insertion of any one of the three bunchers does not alter the transverse characteristics of the beam.

In conclusion, a classical double gap sinusoidal buncher device can be realized to achieve the desired goal of significantly increasing the beam current injected in the cyclotron. However, an original four gap design seems to be particularly advantageous in our case because of the reduced voltage required for bunching, while being indistinguishable from the other possible designs from the particle dynamics point of view. Table 3.1 finally

Number of gaps	2	2	4
Distance between gaps	$3\beta\lambda/2 = 74\,mm$	$\beta\lambda/2 = 25\,mm$	$\beta\lambda/2 = 25\,mm$
Optimal voltage	$750\,V$	$750\,V$	$325\,V$

Table 3.1: Summary of the characteristics of the three types of buncher implementations.

summarizes the characteristics of the three buncher implementations so far compared.

4

THE BUNCHER ELECTRONICS

In the preceding chapter the buncher component was studied from the beam dynamics point of view and the improvement of injection efficiency was evaluated.

For the practical implementation of the device, not only a reliable mechanical design has to be finished (which is outside of the scope of this work) and the mechanical parts have to be machined and assembled in the vacuum chamber, but also the radiofrequency electronic system has to be designed to deliver to the electrodes an oscillating electric signal that meets the required specifications. With some limits the electronics system can be designed independently of the real device, just making some reasonable assumptions.

In the present chapter the buncher electronics system is studied in its building blocks and a number of practical considerations are given for its realization.

4.1 SIGNAL SPECIFICATIONS AND SYSTEM BUILDING BLOCKS

The key specifications of the buncher electric signal were determined.

Firstly, the buncher signal should be locked to the cyclotron signal to the same frequency of 56.16 MHz. Its phase and amplitude should be adjustable at least within an interval of 100 deg and 300 V around the optimal values, which have to be experimentally determined, compensating for any small error between simulation and reality. These intervals are arbitrary but it is reasonable to choose them as large as possible looking at the simulation results of Figure 3.6 in the preceding chapter.

The proposed electronics scheme shown in Figure 4.1 is composed of three parts:

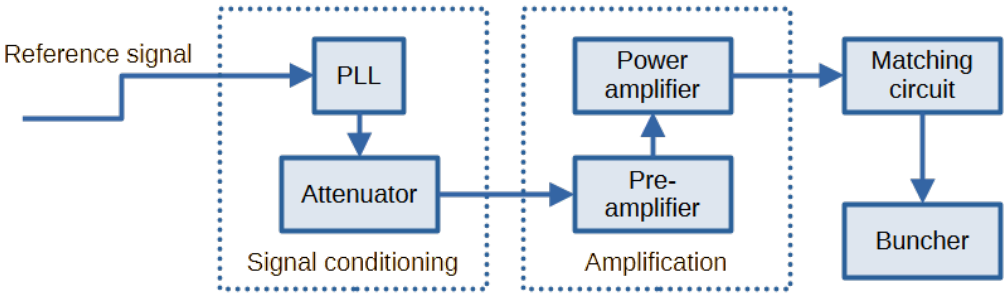

Figure 4.1: Electronics proposal for the buncher device.

1. The signal conditioning block takes as input the reference signal from the cyclotron cavity pick-up and produces a low power signal with the required specifications in terms of phase and amplitude.

2. The amplification block provides power gain to the signal to reach the desired amplitude of electric potential on the buncher electrodes.

3. The impedance matching network is necessary to couple the standard 50 Ω coaxial cable to the purely capacitive load of the buncher, enhancing the amplitude of the signal across the buncher electrodes and avoiding power reflected back to the amplifier.

For completeness, a bi-directional coupler, inserted between the amplification block and the matching circuit, plus a couple of power detectors should be used to measure the direct and the reflected power in order to eventually adjust the matching network components and monitor the system performance.

The buncher device design should also include a pick-up electrode for measuring the actual electric potential on the electrodes.

4.2 SIGNAL CONDITIONING

The signal conditioning block has the scope of generating a low power twin of the cyclotron signal with different phase and amplitude.

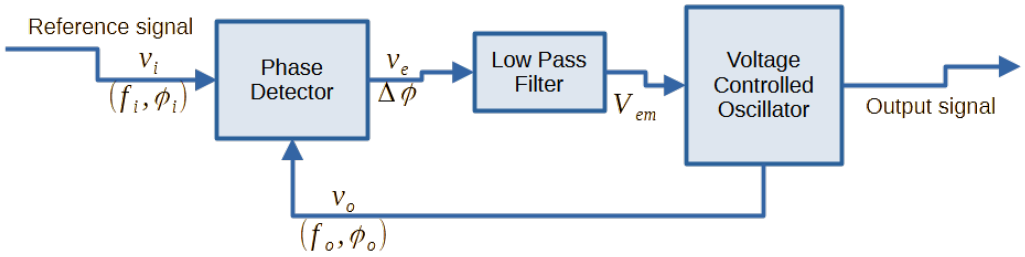

Figure 4.2: PLL schematic.

4.2.1 *Phase Locked Loop*

A phase locked loop (PLL) was recommended to uncouple the cyclotron signal from the following electronic blocks, protecting the subsequent elements from any disturbance.

The scope of this circuit is to generate a twin of the reference signal with identical frequency and a certain fixed phase. The schematic of the circuit is shown in Figure 4.2. It is composed of three components forming a feedback loop.

Basic operation of the loop is now explained, many details can be found in textbooks like [31]. The reference signal v_i with its frequency f_i and phase ϕ_i is continuously compared with the output signal v_o with frequency f_o and phase ϕ_o. The resulting error signal v_e is a function of the phase difference between the output and reference signals $\Delta\phi = \phi_o - \phi_i$. When the reference and the output signals have different frequencies, the phase difference oscillates and consequently the error signal oscillates with a frequency $\Delta f = f_o - f_i$. After necessary filtering, this error signal controls the output signal frequency f_o that is directly proportional to the error level.

When the reference and the output signals goes to the same exactly frequency the error signal stabilizes at a certain DC level proportional to the constant phase difference between the two signals. When eventually the reference signal frequency increases (or decreases) with respect to the output, the error signal increases (or decreases) proportionally, determining an increase of the output frequency. The new output frequency is now closer to the reference and the error signal diminishes. The process repeats until stabilization.

A description of the PLL blocks promptly clarifies the loop operation.

The voltage controlled oscillator (VCO) generates a signal with frequency f_o depending on the input voltage level V_{em} according to its specific transfer function whose plot is reported on the left of Figure 4.3. Basically it represents a direct proportionality between control voltage and output frequency. A certain operating point has to be chosen around which the frequency stability interval will be determined by the low pass filter characteristics. We chose the control voltage of $7.5\,V$ at $55\,MHz$ as the central operating point of our VCO. The ZOS-75 provides a high impedance control input, a main output that produces a signal with $2\,V_{pp}$ amplitude on $50\,\Omega$ load and an auxiliary low power output providing a signal with $300\,mV_{pp}$ amplitude that can be used to feed the phase detector.

The phase detector (PD) produces the error signal by comparing the reference and the output signals. The phase detector circuit used is the commercial Mini Circuit ZRPD-1+ whose architecture is based on a diode ring as reported in the data sheet [32]. It works as a signal mixer which returns the product of two input signals. In our case it is used like a demodulator: two signals very close to each other are given as inputs and at the output a signal at low frequency is observed. For the PD optimal operation it is recommended to use the R input for the low power signal coming from the VCO and the L input for the reference signal whose amplitude should be not lower than $1.4\,V_{pp}$.

Its transfer function was measured by observing the PD output with an oscilloscope while feeding the two inputs with signals reproducing the operational conditions. Both input signals at the frequency of $55\,MHz$, the R signal with amplitude of $300\,mV$ and the L input with amplitude $1.4\,V_{pp}$. The result is reported in the right plot of Figure 4.3. The characteristic is periodic with linear behavior in the region between $40\,deg$ and $140\,deg$.

The PD output feeds the VCO so that its control voltage stabilizes on a value determining an output signal with exactly the same frequency of the reference signal and fixed phase with respect to it. Stability is indeed achieved when the PD output (the error signal) goes to $0\,V$ and the phase between reference and output signals is locked to $90\,deg$. The phase stability interval is the linear range of the PD characteristics between $40\,deg$ and

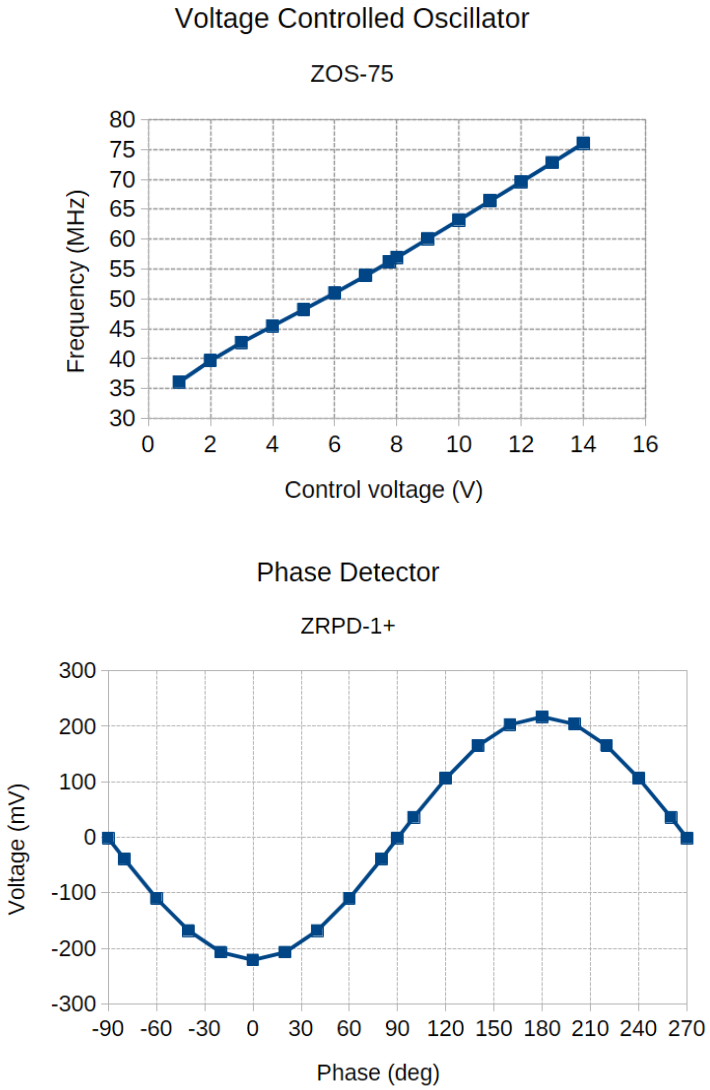

Figure 4.3: Measured VCO (left) and PD (right) transfer functions.

140 *deg*. This means that within that region the stability can be maintained but the signals are locked to a different phase with each other.

The low pass filter is the key element that closes the loop adapting the output of the PD to the input of the VCO. After some attempts, the best configuration was realized with a double stage amplifier using BC337 transistors in common emitter configuration (see Figure 4.4). It performs three tasks at the same time. The use of transistors is necessary to decouple the PD output port from the VCO control input. As seen from their transfer characteristics in Figure 4.3, the operating point of the PD is around 0 *V* while the operating point of the VCO is at 7.5 *V*. The use of transistors make it simple and immediate to shift the PD output and reach the operative point of the VCO without affecting the PD operating point. Furthermore, the transistor works naturally as a low pass filter with no more than few *MHz* passband, cutting the highest frequencies present in the PD output signal. The voltage divider at the input is implemented by a multi-turn potentiometer that can slightly change the bias voltage at the PD output forcing the PD operating point to a value different from 0 *V*, thus allowing regulation of the lock phase within stability limits. The addition of bypass capacitors in parallel with emittance resistors was the solution for increasing the passband and the phase margin of the circuit allowing wider frequency range of stability of the PLL.

The final PLL circuit shown in Figure 4.5 exhibits a 2 *MHz*-wide stability interval around the center frequency of 55.6 *MHz*, the operation frequency of 56.16 *MHz* being safely inside that interval, and the lock phase between reference and output signals can be finely adjusted within 100 *deg* window by changing the potentiometer position. The observed phase error between reference and output signals is less than 3 *deg*. All these characteristics reasonably match the requirements for the buncher.

4.2.2 *Variable attenuator*

In order to control the power level of the buncher signal a variable attenuator can be used like the SYAS+1+ by Mini Circuits [33]. It transmits a signal from the input to the output port attenuating it by a certain factor that depends

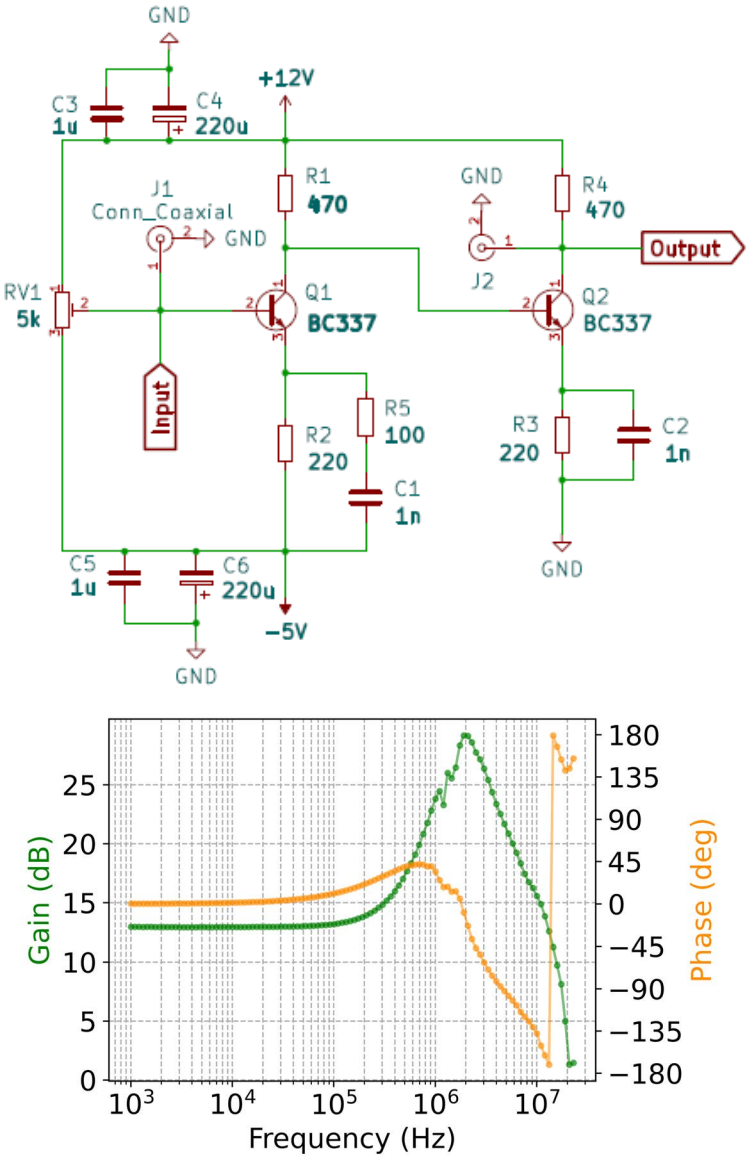

Figure 4.4: Filter schematic and measured gain and phase.

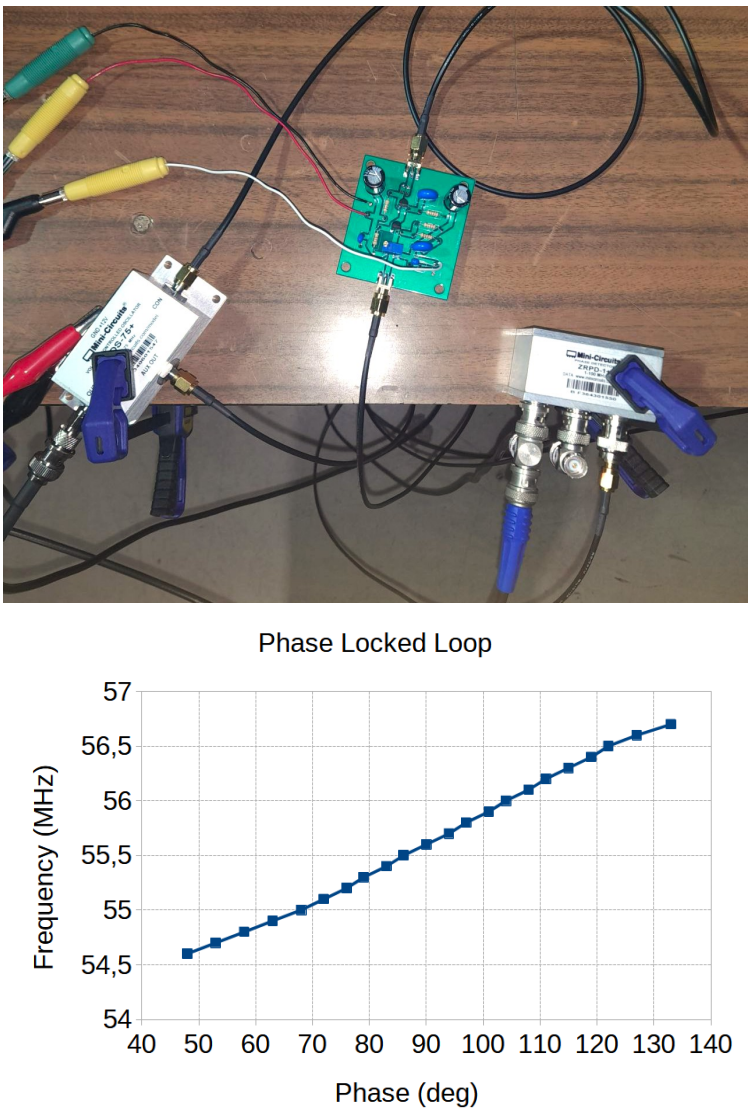

Figure 4.5: Photo of the PLL realized in the laboratory (on the left) and its measured frequency-phase characteristics in the stability range (on the right).

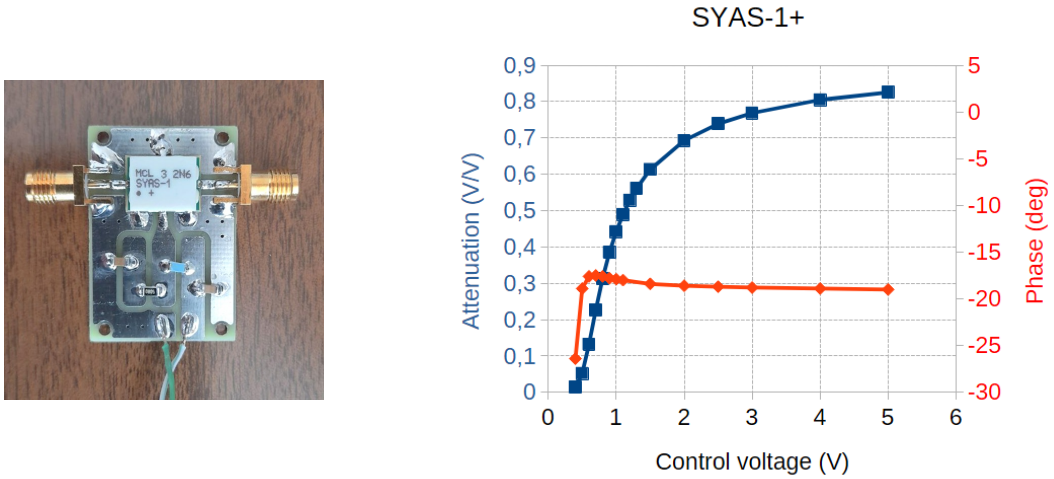

Figure 4.6: Picture of the PCB board for testing the SYAS-1+ component on the left. The circuit was realized according to the recommended scheme of datasheet [33]. The characteristics shown on the right plot were measured with a Vector Network Analyzer setting the stimulus to $0\,dBm$ power in the range from $40\,MHz$ to $70\,MHz$.

on the control voltage level as shown in the plot of Figure 4.6. Unfortunately, the voltage attenuator also changes the phase of the signal.

Other components could also be considered for variable signal attenuation, such as the SVA-2000+ by Mini Circuits [34].

4.3 SIGNAL AMPLIFICATION

For the signal amplification two stages may be required depending on the gain of each stage.

A pre-amplifier takes the low power signal from the previous blocks having $10\,dBm$ maximum rms power and produces a few Watts output capable of driving a high power amplifier to finally reach a power level up to one hundred Watts.

For the pre-amplifier several commercial products can properly do the job, such as the ZHL-10M1G01W0+ by Mini Circuits [35], a wide band amplifier with $22dB$ gain and $1\,W$ ($30\,dBm$) maximum output.

For the power amplifier, the most expensive choice, though the most reliable one, would be to buy a commercial wide band power amplifier, such

as the ZHL-100W-GAN+ by Mini Circuits [36]. With its 42 dB gain it would work alone without any pre-amplifier to achieve the full maximum power of 100 W (50 dBm).

However, a cheaper choice could be worth to be investigated. Based on the transistor MRF300 from NPX, a class-C power amplifier could be designed at the operational frequency like the one reported in the data sheet [37]. Having 27 dB gain, it would necessarily work in combination with the pre-amplifier to reach 300 W, that is more than the needed power.

This class of amplifiers has a narrow pass band and high efficiency of about 80%. They are used for a specific signal frequency as in our case.

Their principle of operation is simple to understand. A power transistor works almost like a switch and excites an LC oscillator load tuned on the signal frequency. Input and output impedance matching networks are necessary to couple the device with input and output transmission lines to get the maximum power gain.

4.4 THE IMPEDANCE MATCHING CIRCUIT

The impedance matching circuit is necessary to couple the buncher device with the amplifier preventing power from being reflected back.

The buncher represents an almost purely capacitive load that have to be transformed into a 50 Ω load to match the transmission line characteristic impedance.

4.4.1 *Principles of impedance matching, transmission lines and Smith chart*

The task of transforming a load impedance to a different equivalent value is accomplished by inserting, between the load and the power source, a number of components, connected in series or in parallel, that could be lumped inductors, capacitors or transmission lines.

The arrangement and value of those components should be computed to give a resulting equivalent impedance equal to the complex conjugated characteristic impedance of the power source for having the maximum power transmission from the source to the load. This is demonstrated in manuals like [38].

A very effective tool for computing the equivalent impedance to achieve the match is the Smith chart. The theory behind this map comes from transmission line theory.

When matching a transmission line (already perfectly matched with a signal source in position $z = 0$) having characteristic impedance Z_0 with a load impedance Z_L located in $z = L$, a reflection coefficient Γ_L can be defined as the ratio between backward and forward voltage (or current):

$$\Gamma_L = \frac{V_{ref}}{V_{inc}} = \frac{Z_L - Z_0}{Z_L + Z_0} = |\Gamma_L| e^{j\theta_L} \tag{4.1}$$

The reflection coefficient in general is a complex number that can be represented in the complex plane with real part on the horizontal axis and imaginary part on the vertical axis. Looking at the polar form, the magnitude of the reflection coefficient is the ratio between reflected and incident voltage amplitude and can take values from 0 (perfect match, no reflected signal) to 1 (total reflection), while the argument θ_L is the phase between reflected and incident signals in $z = L$. When moving backward from the interface by a distance D, we observe the reflection coefficient changing consequently:

$$\Gamma_D = |\Gamma_L| e^{-2\alpha D} e^{j(\theta_L - 2\beta D)} \tag{4.2}$$

Where α is the attenuation constant of the transmission line and β its phase constant. They are both intrinsic characteristics of the transmission line.

When moving backward from the interface between a lossless transmission line ($\alpha = 0$) and the load, it is useful to observe that the reflection coefficient vector consequently rotates in the complex plane by angle $-2\beta D$ from initial angular position θ_L. For a lossy line ($\alpha > 0$) the vector rotates by the same amount but its magnitude diminishes by factor $e^{-2\alpha D}$.

The impedance Z looking in the transmission line at a certain distance D from the interface with the load is defined as the ratio between total voltage $V = V_{ref} + V_{inc}$ over total current $I = I_{ref} + I_{inc}$ and can be expressed in terms of the reflection coefficient Γ:

$$Z = \frac{V}{I} = Z_0 \frac{1 + \Gamma}{1 - \Gamma} = R + jX \tag{4.3}$$

The normalized impedance is simply $Z/Z_0 = r + jx$.

The Smith chart is drawn inside the circle of unit radius in the complex plane where the reflection coefficient $\Gamma = \Gamma_r + j\Gamma_i$ is defined. The chart is formed by the collection of circles of constant resistance r and constant reactance r. These are defined by the following equations derived from 4.3:

$$r = \frac{1 - \Gamma_r^2 - \Gamma_i^2}{(1 - \Gamma_r)^2 + \Gamma_i^2} \tag{4.4}$$

$$x = \frac{2\Gamma_i}{(1 - \Gamma_r)^2 + \Gamma_i^2} \tag{4.5}$$

For completeness we define also the complementary Smith chart starting from the definition of transmission line admittance as the reciprocal of impedance:

$$Y = \frac{I}{V} = \frac{1}{Z} = Y_0 \frac{1 - \Gamma}{1 + \Gamma} = G + jB \tag{4.6}$$

whose real part G is called the conductance and the imaginary part B the susceptance. Following analogous algebra steps we can define the normalized admittance $y = Y/Y_0 = g + jb$ and then the circles with constant conductance g and constant susceptance b. They results to be the same as those defined previously for constant r and x but mirrored with respect to the imaginary axis.

In Figure 4.7 the complete Smith chart is reproduced showing the circles with constant r and x in red and those with constant g and b in blue. This is the normalized Smith chart. In the practical case of any characteristic impedance Z_0, we can set the circle labels to $R = r \cdot Z_0$, $X = x \cdot Z_0$, $G = g/Z_0$, $B = b/Z_0$ to obtain a more practical, though not general, Smith chart for the specific case.

Now, the so defined Smith chart can be directly used to design an impedance matching circuit with a step by step process.

We start connecting the signal source with its characteristic output impedance Z_S directly to the load Z_L and representing the reflection coefficient $\Gamma = \frac{Z_L - Z_S}{Z_L + Z_S} = \Gamma_r + j\Gamma_i$ as a point in the Smith chart. We usually work with a source having characteristic output impedance of $Z_S = 50\,\Omega$.

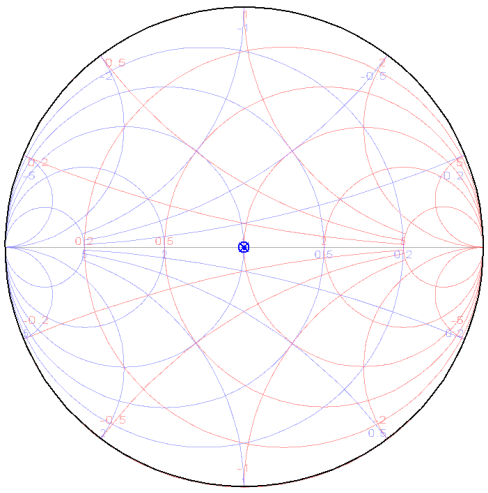

Figure 4.7: Complete normalized Smith chart is obtained by superposition of four families of circles with constant r and x (in red), g and b (in blue). The central point is associated with perfect match between source and load leading to null reflection coefficient.

The desired perfect match between the source and the load is achieved when the reflection coefficient looking into the matching circuit connected to the load is equal to zero and it is represented as the origin point of the Smith chart.

The game is now to add between the source and the load the necessary elements to make the reflection coefficient move from its initial position to the center of the Smith chart.

The main rules are:

- As already explained, inserting a piece of transmission line of length D with certain characteristic parameters α and β makes the reflection coefficient rotate clockwise by angle $2\beta D$ and reducing by factor $e^{-2\alpha D}$.
- Inserting a series capacitor C (or inductor L) makes the point move counterclockwise (or clockwise) on the circle of constant resistance by the amount $\Delta X = \frac{1}{\omega C}$ (or $\Delta X = \omega L$), ω being the angular frequency of the signal.
- Inserting a parallel capacitor (or inductor) makes the point move clockwise (or counterclockwise) on the circle of constant conductance by the amount $\Delta B = \omega C$ (or $\Delta B = \frac{1}{\omega L}$).

- Inserting a series (or parallel) resistor R makes the point move on the circle of constant reactance (or susceptance) towards the real axis.

Also some pieces of short-circuited or open transmission lines with characteristic impedance Z_0 and propagation parameters α and β can be added in series or in parallel to modify the reflection coefficient. Such line pieces are called stubs and can be used to achieve impedance matching. The rules for navigating in the Smith chart by adding stubs are:

- Insertion of an open (or short-circuited) parallel stub makes the reflection coefficient move clockwise (or counterclockwise) on the constant conductance circle depending on stub length.
- Insertion of an open (or short-circuited) series stub makes the reflection coefficient move counterclockwise (or clockwise) on the constant resistance circle depending on stub length.

The game can be played with pen and paper, but using a suitable software makes it faster and easier to calculate the values of components (capacitance, inductance, resistance and parameters of a transmission line) required for the matching circuit.

4.4.2 *The buncher matching network*

To design the matching circuit for the buncher we need to know the impedance of the device. Looking at the ideal mechanical designs presented in the previous chapter (Figure 3.3 and Figure 3.11) we understand that the device can be considered in first approximation as a pure capacitor. However, the exact value of capacitance strongly depends on how the component is realized in practice.

The buncher electrodes need a mechanical structure keeping them together in the correct position inside the vacuum chamber. The details of this structure have not been defined yet, but for the scope of the present work a reasonable structure can be imagined in order to calculate a reference value of capacitance that we may expect.

The design proposed in Figure 4.8 embeds the electrodes in a grounded box to both mechanically sustain the electrodes and keep them in the correct

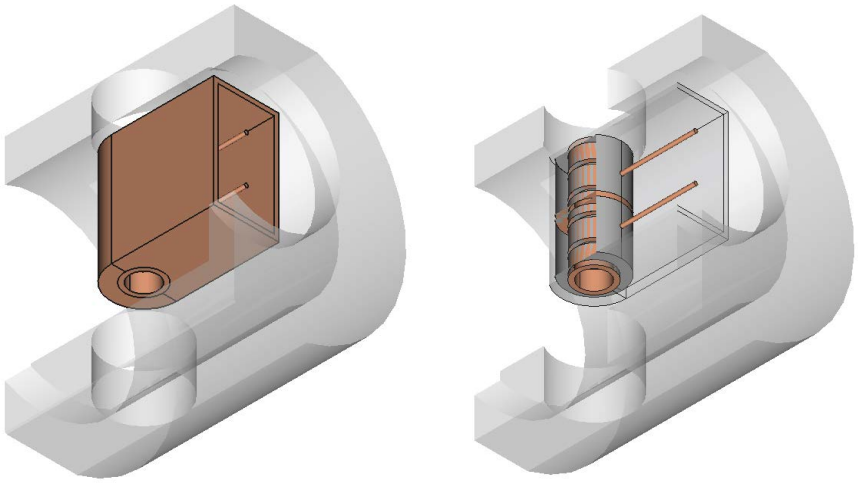

Figure 4.8: Idea of a simple mechanical structure design of the buncher as it would appear in the vacuum chamber. Though not detailed, the drawing is necessary to give an order of magnitude of the buncher capacitance.

position but also shield the electric fields from the surrounding. The ground electrodes are directly welded to the box, while the two electrodes bringing the oscillating potential are enveloped by two plastic insulators that both keep them in position and prevent them from touching the ground surfaces. The ground box also make the component impedance almost independent of the surrounding and easy to calculate with some rough assumptions, though leading to reasonable values. Indeed, no expensive simulations are worth at this stage of the component development, because the real impedance of the device must be measured in practice once it will be built.

The capacitance of any conductor system is determined by conductors set at different potentials facing to each other by some distance filled with a dielectric material. In first approximation the basic formula of the plane capacitor can be used neglecting fringing fields. The capacitance is defined as the charge Q accumulated on each conductor over voltage difference ΔV and it is proportional to the facing surface S of the conductors and inversely proportional to the distance d between them:

$$C = \frac{Q}{\Delta V} = \epsilon_0 \epsilon_r \frac{S}{d} \tag{4.7}$$

the relative dielectric constant ϵ_r being dependent on the material used for filling the space between conductors.

In our case the buncher capacitance takes the most important contribution from the lateral surface of the two electrodes. Looking at the design in Figure 4.8, we can consider that surface S being two times the half of an ideal cylindrical surface placed in the middle between one electrode and the ground shell:

$$S = 2\pi R_m L \tag{4.8}$$

the R_m being the mean radius between external electrode radius fixed at $20\,mm$ and the internal shell radius (variable). The length L of the electrodes is half the characteristic buncher length $d_0/2 = 24.5\,mm$.

For our range of geometrical parameters, this way of calculation gives a good agreement (less than $1\,pF$ deviation) with respect to the implementation of the well known cylindrical capacitor formula.

With all those assumptions the value of buncher capacitance can be estimated with respect to the distance between inner and outer electrodes and to the value of relative dielectric constant. The results are shown in Figure 4.9 using some reasonable values for the dielectric constant and for electrode distance. The behavior of capacitance as a function of distance shows that below $10\,mm$ the variation of capacitance tends to be negligible compared to the distance increment, so we can assume this distance as a reference for the design with the aim of keeping the buncher capacitance as little as possible. With this choice of $10\,mm$ spacing and a medium value of dielectric constant of $\epsilon_r = 3$ we get the reference value of $10\,pF$ for the buncher capacitance.

Considering all the range of values for the buncher capacitance, a design of the matching circuit can be now elaborated.

Among several solutions, we take as a template the one realized by Risto Kronholm and Taneli Kalvas for the cyclotron MCC30 [39] [40] at University of Jyväskylä, Finland, presented in the ECPM2024 conference [41].

As Smith chart software package for the design of the matching circuit we chose SimNEC that is freely available on the official website[1].

The idea behind the design is to use a piece of transmission line plus two adjustable capacitors to achieve the impedance match to the target $50\,\Omega$

1 https://www.ae6ty.com/smith_charts/

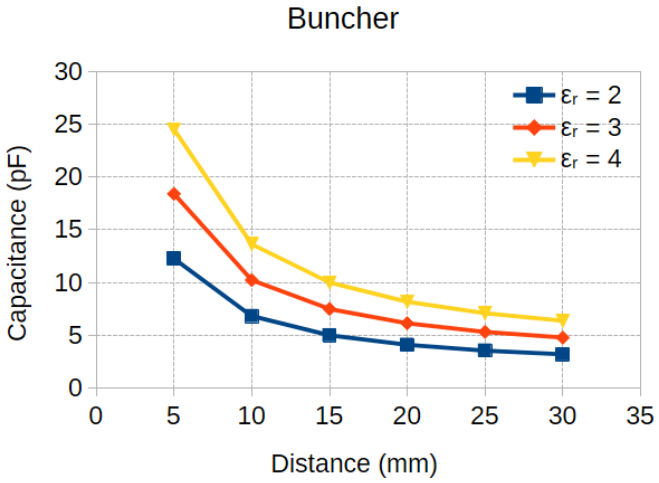

Figure 4.9: Buncher capacitance as function of distance between inner electrodes and outer shell computed for different values of relative perimittivity ϵ_r of the insulator material.

(see Figure 4.10). The design offers two main advantages. Because of very little space near our vacuum chamber in the injection line of the cyclotron, a piece of transmission line is necessary to locate all the other components far from the buncher. Moreover, the use of adjustable capacitors makes the system very flexible to be adapted to several possible values of buncher capacitance and also takes into account any eventual variation during the device operation.

The 90 *deg* shift transmission line is used as an inductor to transform the capacitive load into an inductive load moving the representative point from a negative to a positive reactance circle. Due to transmission line attenuation coefficient, the reflection coefficient also moves on a non null resistance circle. Now a parallel capacitor $C1$ is used to locate the point on the $50\,\Omega$ circle and finally a series capacitor $C2$ cancels the reactive part of the impedance reaching the center of the Smith diagram. A parallel $500\,\Omega$ resistor can be added just in front of the signal source to limit the reflection coefficient when eventually the system would run away from perfect match thus protecting the power amplifier.

The software also computes the voltage across the terminals of each element. In particular we are interested to know the voltage required from the power source to produce the desired voltage across the buncher electrodes.

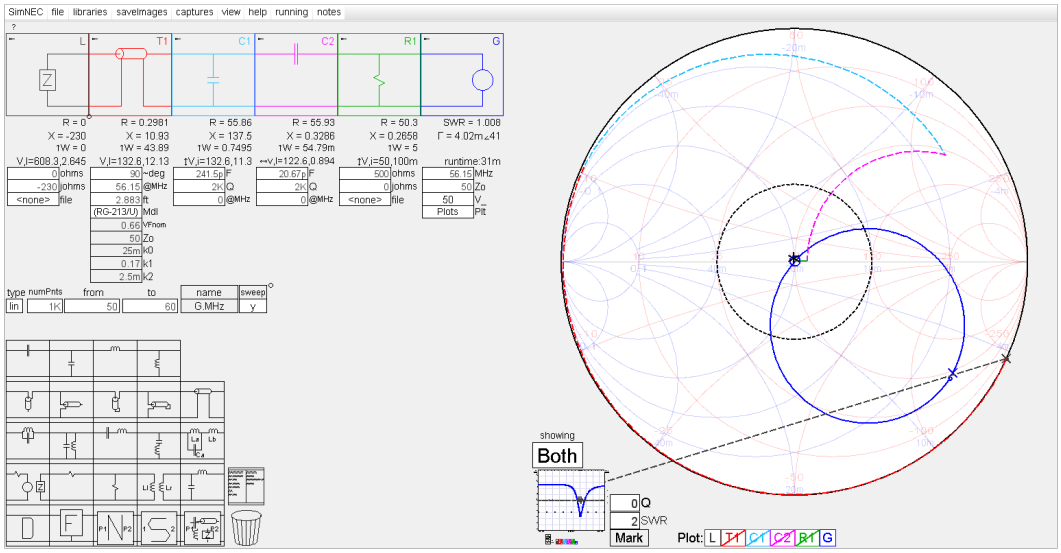

Figure 4.10: Matching circuit for 10 pF buncher capacitance and corresponding Smith chart as it appears in the SimNEC graphical user interface.

We can simply define a voltage transforming ratio of the matching circuit as the ratio between the output voltage over the input voltage. In our case it is around 12 so that the input voltage is multiplied by that factor when going from the source to the buncher through the matching circuit.

In the case of a double gap buncher the desired target is 750 V (525 V rms) that would require 43 V rms or 37 W input power. Instead, in the case of a four gap buncher an input signal of 22 V rms amplitude would be sufficient to have the required 265 V rms ampltude on the buncher electrodes, the needed power being 10 W.

The power needed for having the desired potential on the buncher electrodes should be added to the power required for beam bunching that can be computed by multiplying the beam current intensity (maximum 6 mA) by the rms kinetic energy variation of 525 eV, being in the order of few Watts at maximum.

Although we expect the total power required by the buncher operation to be in the order of tens of Watts, for a reliable long term operation of the system an amplifier is recommended with maximum power at least the double of the needed.

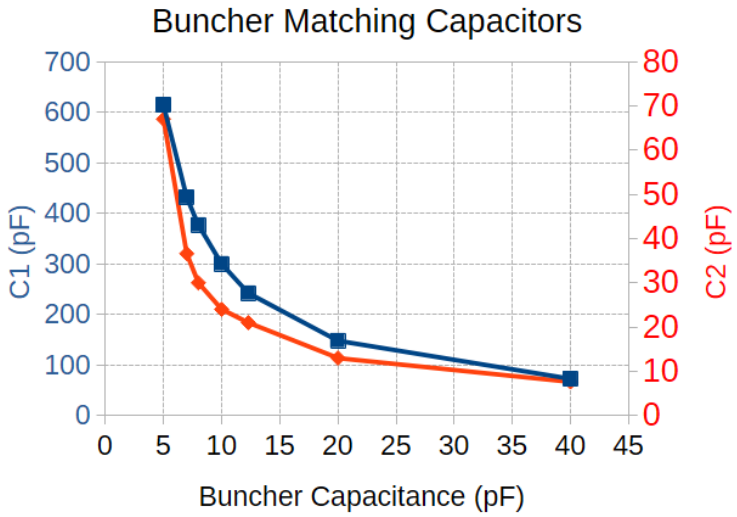

Figure 4.11: The matching capacitor values $C1$ and $C2$ required for achieving the impedance match as functions of the buncher capacitance.

We can finally vary the buncher capacitance over a large interval from 5 pF to 40 pF and find the value of capacitors $C1$ and $C2$ necessary to achieve the impedance match. The result is reported in Figure 4.11. This is useful to have an idea of how much the value of the capacitors would change with the buncher capacitance and also helps in the choice of the correct components.

For the most reliable operation the use of adjustable vacuum capacitors is recommended to achieve the best stability of the matching circuit.

5

CONCLUSIONS

The present work sees the complete development of a buncher device to improve the beam injection efficiency in the cyclotron of SPES project at Legnaro National Laboratories.

The perspective of SPES project is to create a new facility in Italy for the production of exotic isotopes for various applications ranging from fundamental nuclear studies up to the search of novel isotopes for nuclear medical applications, both therapy and diagnostics, and potentially massive production of such isotopes.

The core of the facility is a high intensity cyclotron that provides two proton beams with combined maximum intensity of $700\,\mu A$ and energy from $35\,MeV$ to $70\,MeV$.

The beam injection in the cyclotron is crucial for optimal operation of the machine and this work is devoted to study the achievable improvement of injection efficiency of beam in the cyclotron for its better operation.

The study of the existing systems (the low energy beam transport line and the cyclotron central region) has been carried out in the first part of this work (Chapters 1 and 2) employing computer simulations of the multi-particle dynamics in the electromagnetic fields and comparing the results with the experimental data obtained during cyclotron operations. The focus of Chapter 1 is on the transverse beam dynamics in the injection line that transports the H^- ions from the ion source exit up to the inflector entrance by means of several magnetostatic elements. The scope there was to reproduce with the aid of computer simulations the characteristics of the beam along the line. Chapter 2 is devoted to the beam dynamics in the central region of the cyclotron, in particular the longitudinal dynamics in the first few turns of beam inside the machine. This represents the necessary step to delve deeper into the concept of phase acceptance and the mechanism of beam injection in the cyclotron. The first turn is indeed the crucial part of beam trajectory, where actually only the 14 % of all the initial particles are selected

for further acceleration within about 60 *deg* of maximum phase acceptance interval.

To enhance the cyclotron injection efficiency a beam bunching system is necessary. The existing beam transport line only accounts for transverse matching of the beam to the cyclotron entrance. A bunching device would improve the longitudinal matching of the beam by periodically compressing it, thus forming groups of ions (bunches) that enter the cyclotron within its phase acceptance window.

The optimal buncher design has been defined by studying the device from its operation principles and employing computer simulations to estimate the improvement of injection efficiency and finally comparing several design solutions to choose the most favorable one. The noticeable result found is that at least the double of the actual beam current would be accepted into the cyclotron by using the buncher device (up to 35 % transmission in the central region at low beam currents). Also the space charge effects on the beam dynamics in the first turn into the cyclotron were simulated to take into account the non-negligible intensity of the injected beam (up to 6 mA of current provided by the ion source). Because of ion-ion repulsion at low energy, the bunching efficiency degrades by few % every mA of current increase. Moreover, from the comparison of several designs, an original four-gap buncher emerged as an advantageous configuration because the voltage necessary for its optimal operation is lower than required by the classical two-gap device, while beam dynamics does not differ significantly among the compared designs.

Part of the results presented up to this point can be found in the recent publication [42].

The last part of the work contains a proposal of implementation of the electronic chain needed for the reliable operation of the buncher device. Each part of the system is studied and some practical attempts and calculations were done to demonstrate the effectiveness of the solutions presented. In particular, the conditioning of the signal provided by the cyclotron radiofrequency system was treated and a phase locked loop circuit was realized to achieve the desired specifications in terms of phase and voltage adjustment. Finally, an impedance matching circuit for connecting the buncher device to

the power amplifier was also designed to provide the necessary voltage on the buncher electrodes without power reflection.

BIBLIOGRAPHY

[1] T Marchi et al. "The SPES facility at Legnaro National Laboratories." en. In: *Journal of Physics: Conference Series* 1643.1 (Dec. 2020), p. 012036. ISSN: 1742-6588, 1742-6596. DOI: 10.1088/1742-6596/1643/1/012036. URL: https://iopscience.iop.org/article/10.1088/1742-6596/1643/1/012036 (visited on 10/06/2025).

[2] Gaia Pupillo et al. "Cyclotron-based production of innovative medical radionuclides at the INFN-LNL: state of the art and perspective." en. In: *The European Physical Journal Plus* 138.12 (Dec. 2023), p. 1095. ISSN: 2190-5444. DOI: 10.1140/epjp/s13360-023-04564-3. URL: https://link.springer.com/10.1140/epjp/s13360-023-04564-3 (visited on 11/25/2025).

[3] D. Manura and D. Dahl. *SIMION 8.1 User Manual*. Palmer, MA: Adaptas Solutions, LLC, 2008. URL: https://simion.com/.

[4] D. C. Faircloth. *Particle Sources*. arXiv:2103.13231 [physics]. Mar. 2021. DOI: 10.48550/arXiv.2103.13231. URL: http://arxiv.org/abs/2103.13231 (visited on 11/17/2025).

[5] Bin Wang, Wenzhong Shi, and Zelang Miao. "Confidence Analysis of Standard Deviational Ellipse and Its Extension into Higher Dimensional Euclidean Space." en. In: *PLOS ONE* 10.3 (Mar. 2015). Ed. by Duccio Rocchini, e0118537. ISSN: 1932-6203. DOI: 10.1371/journal.pone.0118537. URL: https://dx.plos.org/10.1371/journal.pone.0118537 (visited on 11/18/2025).

[6] Wolfgang Hillert. "Transverse Linear Beam Dynamics." en. In: *Proceedings of the CERN–Accelerator–School course: Introduction to Accelerator Physics*. arXiv:2107.02614 [physics]. Dec. 2021, p. 65. DOI: 10.48550/arXiv.2107.02614. URL: http://arxiv.org/abs/2107.02614.

[7] Francis Labrecque. *Injection Line Design*. en. 2014.

[8] Paul W. Allison, Joseph D. Sherman, and David B. Holtkamp. "An Emittance Scanner for Intense Low-Energy Ion Beams." en. In: *IEEE Transactions on Nuclear Science* 30.4 (Aug. 1983), pp. 2204–2206. ISSN: 0018-9499. DOI: 10.1109/TNS.1983.4332762. URL: http://ieeexplore.ieee.org/document/4332762/.

[9] P Royer. *Solenoidal Optics*. Tech. rep. CERN-OPEN-2000-324, CERN-NEUTRINO-FACTORY-Note-11, CERN-NUFACT-Note-11, CERN-PS-HP-Note-99-12. Geneva: CERN, 1999. URL: https://cds.cern.ch/record/479729.

[10] Martin Reiser. *Theory and Design of Charged Particle Beams*. en. 1st ed. Wiley, Mar. 2008. ISBN: 978-3-527-40741-5 978-3-527-62204-7. DOI: 10.1002/9783527622047. URL: https://onlinelibrary.wiley.com/doi/book/10.1002/9783527622047 (visited on 11/06/2025).

[11] Vinit Kumar. "Understanding the focusing of charged particle beams in a solenoid magnetic field." en. In: *American Journal of Physics* 77.8 (Aug. 2009), pp. 737–741. ISSN: 0002-9505, 1943-2909. DOI: 10.1119/1.3129242. URL: https://pubs.aip.org/ajp/article/77/8/737/310817/Understanding-the-focusing-of-charged-particle.

[12] Mario Conte and William W. McKay. *An introduction to the physics of particle accelerators*. en. 2nd ed. Singapore: World scientific, 2008. ISBN: 978-981-277-960-1.

[13] Cristhian A. Valerio-Lizarraga, Ildefonso Leon-Monzon, and Richard Scrivens. "Negative ion beam space charge compensation by residual gas." en. In: *Physical Review Special Topics - Accelerators and Beams* 18.8 (Aug. 2015), p. 080101. ISSN: 1098-4402. DOI: 10.1103/PhysRevSTAB.18.080101. URL: https://link.aps.org/doi/10.1103/PhysRevSTAB.18.080101.

[14] R Baartman and D Yuan. "Space charge neutralization studies of an H- beam." In: Rome, 1988.

[15] Alberto Ruzzon, Mario Maggiore, Arturo Abbondanza, Piergiorgio Antonini, and Lorenzo Pranovi. "Design of an E × B Chopper System Based on Permanent Magnets for the Injection Line of the SPES Project Cyclotron." en. In: *Instruments* 9.2 (Apr. 2025), p. 10. ISSN: 2410-390X.

DOI: 10.3390/instruments9020010. URL: https://www.mdpi.com/2410-390X/9/2/10 (visited on 11/17/2025).

[16] P. Heikkinen. "Injection and extraction for cyclotrons." English. In: *CAS CERN accelerator school: 5. general accelerator physics course. Vol. 2. Proceedings*. Jyväskylä, Finland, 1994, pp. 819–839. ISBN: 92-9083-058-1. URL: https://inis.iaea.org/records/8shq3-p2m32.

[17] Dragan Toprek. "Theory of the central ion trajectory in the spiral inflector." en. In: *Nuclear Instruments and Methods in Physics Research Section A: Accelerators, Spectrometers, Detectors and Associated Equipment* 440.2 (Feb. 2000), pp. 285–295. ISSN: 01689002. DOI: 10.1016/S0168-9002(99)00859-1. URL: https://linkinghub.elsevier.com/retrieve/pii/S0168900299008591 (visited on 11/17/2025).

[18] John J. Livingood. *Principles of cyclic particle accelerators*. en. D. Van Nostrand Company, inc., 1961.

[19] V. L. Smirnov. "The Cyclotron and Its Modeling." en. In: *Physics of Particles and Nuclei* 52.5 (Sept. 2021), pp. 913–996. ISSN: 1063-7796, 1531-8559. DOI: 10.1134/S106377962105004X. URL: https://link.springer.com/10.1134/S106377962105004X (visited on 10/08/2025).

[20] F Chautard. "Beam dynamics for cyclotrons." en. In: Zeegse, The Netherlands: CERN, 2006, pp. 209–229. DOI: 10.5170/CERN-2006-012.209. URL: http://cds.cern.ch/record/1005052 (visited on 11/17/2025).

[21] Mike Seidel. "Cyclotrons and Fixed Field Alternating Gradient Accelerators." en. In: *Proceedings of the CERN–Accelerator–School course: Introduction to Accelerator Physics*. arXiv:2105.04477 [physics]. Dec. 2021, p. 20. DOI: 10.48550/arXiv.2105.04477. URL: http://arxiv.org/abs/2105.04477 (visited on 11/17/2025).

[22] P Heikkinen. "Cyclotrons." en. In: Jyväskylä, Finland: CERN, 1994, pp. 805–818. DOI: 10.5170/CERN-1994-001.805. URL: http://cds.cern.ch/record/398438.

[23] W Kleeven. "Injection and extraction for cyclotrons." en. In: Zeegse, The Netherlands: CERN, 2006, pp. 271–296. DOI: 10.5170/CERN-2006-012.271. URL: http://cds.cern.ch/record/1005057 (visited on 11/27/2025).

[24] J. Saario, J. Gustafsson, P. Kotilainen, K. Kaski, A. Lassila, and E. Liukkonen. "Beam buncher for the K130-cyclotron." en. In: *Nuclear Instruments and Methods in Physics Research Section A: Accelerators, Spectrometers, Detectors and Associated Equipment* 370.2-3 (Feb. 1996), pp. 330–334. ISSN: 01689002. DOI: 10.1016/0168-9002(95)00847-0. URL: https://linkinghub.elsevier.com/retrieve/pii/0168900295008470 (visited on 10/03/2025).

[25] Zhiyu Wang, Zhiguang Qiao, Wei Liu, Xiaowei Cai, Qiong Wu, Haoran Fu, Jiebin Luo, Haipeng Li, and Sheng Wang. "Development of sawtooth waveform beam buncher for medical cyclotron accelerator." en. In: *Review of Scientific Instruments* 96.2 (Feb. 2025), p. 023306. ISSN: 0034-6748, 1089-7623. DOI: 10.1063/5.0251414. URL: https://pubs.aip.org/rsi/article/96/2/023306/3337334/Development-of-sawtooth-waveform-beam-buncher-for (visited on 10/03/2025).

[26] H. von Jagwitz, U. Hagen, O. Heid, and S. Setzer. "Low Energy Bunching with a Double Gap RF Buncher." en. In: *Proceedings of IPAC2011*. Vol. 110904. San Sebastián, Spain, 2011, pp. 1725–1727. URL: https://proceedings.jacow.org/IPAC2011/papers/tups080.pdf.

[27] Tea Gun Yang et al. "Development of a Beam Buncher for the KIRAMS-30 Cyclotron." en. In: *Journal of the Korean Physical Society* 56.6(1) (June 2010), pp. 1960–1963. ISSN: 0374-4884. DOI: 10.3938/jkps.56.1960. URL: http://www.jkps.or.kr/journal/DOIx.php?id=10.3938/jkps.56.1960 (visited on 10/03/2025).

[28] W.J.G.M. Kleeven, W. Gelbart, and J. Sura. "Optical properties of a two-gap buncher." en. In: *Nuclear Instruments and Methods in Physics Research Section B: Beam Interactions with Materials and Atoms* 64.1-4 (Feb. 1992), pp. 367–370. ISSN: 0168583X. DOI: 10.1016/0168-583X(92)95496-E. URL: https://linkinghub.elsevier.com/retrieve/pii/0168583X9295496E (visited on 10/03/2025).

[29] V. S. Pandit, P. R. Sarma, and R. K. Bhandari. "Optimization of the parameters of an ion beam buncher." en. In: *Nuclear Instruments and Methods in Physics Research Section A: Accelerators, Spectrometers, Detectors and Associated Equipment* 276.1–2 (1989), pp. 21–24. ISSN: 0168-9002. DOI:

10.1016/0168-9002(89)90610-4. URL: https://www.sciencedirect.com/science/article/pii/0168900289906104.

[30] David Alesini. "Linac." In: Version Number: 1. arXiv, 2021. DOI: 10.48550/ARXIV.2103.16500. URL: https://arxiv.org/abs/2103.16500 (visited on 11/17/2025).

[31] William F. Egan. *Phase-Lock Basics*. en. 1st ed. Wiley, Oct. 2007. ISBN: 978-0-470-11800-9 978-0-470-17873-7. DOI: 10.1002/9780470178737. URL: https://onlinelibrary.wiley.com/doi/book/10.1002/9780470178737 (visited on 11/06/2025).

[32] Mini Circuits. *Phase Detector*. URL: https://www.minicircuits.com/pdfs/ZRPD-1+.pdf.

[33] Mini Circuits. *Attenuator/Switch*. URL: https://www.minicircuits.com/pdfs/SYAS-1+.pdf.

[34] Mini Circuits. *Voltage Variable Attenuator*. URL: https://www.minicircuits.com/pdfs/SVA-2000+.pdf.

[35] Mini Circuits. *Medium Power Amplifier*. URL: https://www.minicircuits.com/pdfs/ZHL-10M1G01W0+.pdf.

[36] Mini Circuits. *High Power Amplifier*. URL: https://www.minicircuits.com/pdfs/ZHL-100W-GAN+.pdf.

[37] NXP Semiconductors. *RF Power LDMOS Transistors*. English. June 2019. URL: https://www.nxp.com/docs/en/data-sheet/MRF300AN.pdf.

[38] Samuel Y. Liao. *Microwave devices and circuits*. eng. 3. ed. Prentice Hall international editions. Englewood Cliffs: Prentice-Hall, 1990. ISBN: 978-0-13-583204-2 978-0-13-584681-0.

[39] P M T Heikkinen. "Commissioning of the JYFL MCC30/15 Cyclotron." en. In: Lanzhou, China, 2010.

[40] P Heikkinen. "New Mcc30/15 Cyclotron For The Jyfl Accelerator Laboratory." en. In: 2007.

[41] Taneli Kalvas. *Commissioning of the Jyväskylä MCC30*. en. Jyväskylä, Finland, May 2024.

[42] Arturo Abbondanza, Mario Maggiore, Piergiorgio Antonini, Lorenzo Pranovi, and Alberto Ruzzon. "Study of the injection system of SPES cyclotron and development of a buncher device." en. In: *Journal of Instrumentation* 20.06 (June 2025), P06056. ISSN: 1748-0221. DOI: 10.1088/1748-0221/20/06/P06056. URL: https://iopscience.iop.org/article/10.1088/1748-0221/20/06/P06056 (visited on 11/17/2025).

COLOPHON

This document was typeset using the typographical look-and-feel `classicthesis` developed by André Miede and Ivo Pletikosić. The style was inspired by Robert Bringhurst's seminal book on typography "*The Elements of Typographic Style*". `classicthesis` is available for both LaTeX and LyX:

https://bitbucket.org/amiede/classicthesis/

Final Version as of January 23, 2026 (classicthesis v4.6).